PARABOLIC EQUATION SOLUTION FOR A TRANSITIONAL SOLID SEAFLOOR

by

Eric James Threet

A thesis submitted to the Faculty and the Board of Trustees of the Colorado School of Mines in partial fulfillment of the requirements for the degree of Master of Science (Mathematical and Computer Sciences).

Golden, Colorado

Date _____

Signed: _____
Eric James Threet

Signed: _____
Dr. Jon Collis
Thesis Advisor

Golden, Colorado

Date _____

Signed: _____
Dr. Willy Hereman
Professor and Head
Department of Applied Mathematics and Statistics

ABSTRACT

The study of sound propagation in the ocean has a wide range of applications and is interesting from a mathematical perspective. Parabolic equation solutions, resulting from factoring the parabolic wave equation, have been formulated for sound propagation in a variety of propagation environments. In this work, an idealized environment, that of a water layer, overlying a denser fluid sediment layer (termed a transitional solid), overlying an elastic basement is considered. Parabolic equation solutions for the acoustic pressure field are advantageous as they accurately handle range dependence and are computationally efficient. Using rational-linear approximations for the depth operator, which arises in the parabolic factorization, in an azimuthally symmetric outgoing wave equation gives accurate and efficient results for wide propagation angles. Parabolic equation solutions for sound propagation in the ocean differ in their treatment of the layered seafloor. Solutions that treat the sediment as a fluid and elastic, poro-elastic, and poro-acoustic solids are in use. An improved model is developed and implemented for a stratified environment with transitional solid sediments, sediments that may accurately be treated as a fluid. This involves strictly enforcing interface conditions, accomplished numerically by eliminating nonphysical values that appear near the interface in a Galerkin-inspired discretization of a parabolic equation range-marching solution. The implementation is verified by comparing it to existing models that treat the sediment as a fluid or as an elastic solid. Comparisons are drawn between fluid, elastic, and poro-elastic sediment treatments.

TABLE OF CONTENTS

LIST OF FIGURES

ACKNOWLEDGMENTS

Deepest Thanks To:

- My parents, Mary Ann and Randy Threet. Their constant love and support is the wind and sun on my back, driving me forward, keeping me warm.
- My sister Emily and the rest of my big happy family, my foundation.
- Doctor Jon Collis, my advisor, mentor, and friend. I strive to follow his example in academia and outside of it.
- Professors Bernard Bialecki and Paul Martin, my thesis committee members and most revered instructors. True mathematicians, gentlemen, and scholars.
- The faculty and staff of the Colorado School of Mines, especially Holly Eklund, Terry Bridgman, Angel Abbud-Madrid, Tina Gianquitto, and Yong Bakos.
- All my past teachers who gave me more than knowledge, who sparked my creativity and expected greatness.
- My dearest friends: Emerson Lawrence and the gang, Lauren Howell and my fellow math graduate students, the gents of Bradford Second, Team Wades Garage, and my fellow staffers of Camp Alexander.

For Uncle Mike

CHAPTER 1

INTRODUCTION

The study of sound waves, or acoustics, has been a historical topic of interest for many mathematicians and physicists. D'Alembert published his formulation of the wave equation in 1747. Sound propagation in a fluid was first described by Newton in his 1687 *Principia Mathematica*. The speed of sound in water was first accurately measured by Sturm and Colladen in Lake Geneva, Switzerland in 1826. Sound waves are known to propagate better in the ocean than any other type of wave or radiation. Under the proper conditions which are most common in deep oceans away from the poles, sound can travel very far in the water. The ability of sound to travel efficiently and to great distances in the ocean makes acoustic prediction a strong tool for studying the oceanography of the water column and geography of the seafloor. Similar to optics, the study of acoustics benefits from both wave and ray models. Advances in computer technology have improved the study of underwater acoustics in every way, increasing the detail, accuracy, and scope of any investigation, for substantially less money than field experiments [1].

The ocean is an incredibly complex physical environment, with a wide range of influences on sound propagation. The speed of sound in the the ocean is a function of temperature, salinity, and depth. All of these factors are dependent on the geography of the region, time of day, month, and year, and other influences on the ocean environment. Near the surface is a well mixed isothermal layer resulting from wind and wave activity. Below this layer, in typical nonpolar regions, is a thermocline where temperature, and thus sound speed, decrease as depth increases. Due to thermodynamic properties of salt water under pressure, the water temperature decreases slowly from 4°C below the thermocline. Sound speed increases with pressure from this point on down, leaving a distinct region of low sound speed, the deep sound

channel, as seen in 1.1. Sound refracts toward regions of minimum sound speed, according to Snell's Law, so sound travels to the greatest distances in the deep sound channel. In polar regions, cold surface water prevents the existence of a deep sound channel, and sound speed increases with depth from the surface.

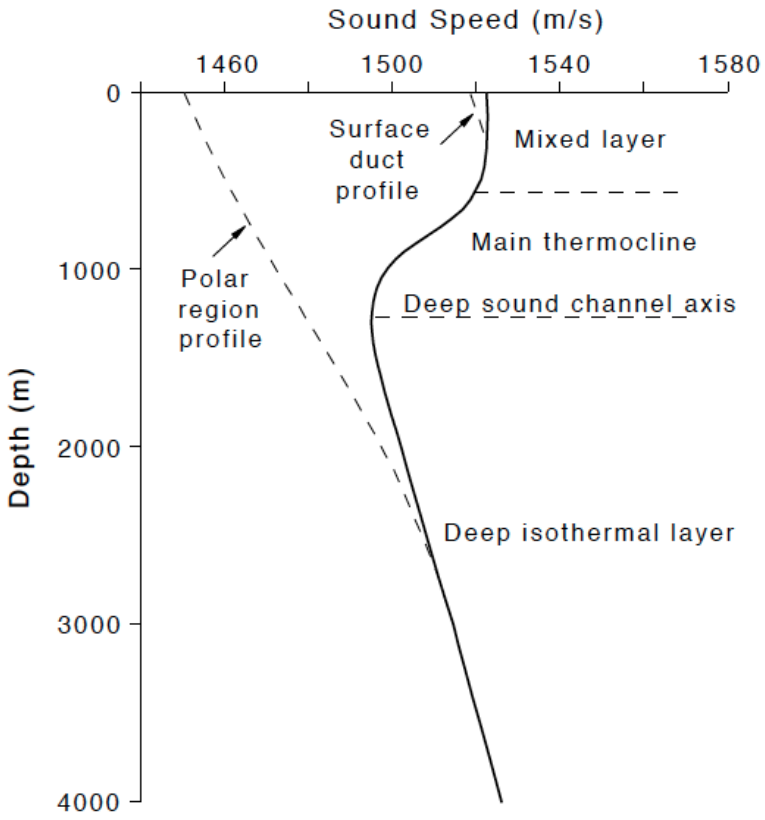

Figure 1.1: Generic Sound Speed Profile

The seafloor and ocean surface bound the acoustic waveguide that is the ocean, causing reflection, scattering, attenuation, and transmission of sound waves. Sound waves may penetrate the seafloor; so the propagation environment includes the water, sediment layers, and underlying rock layers. Underwater sound propagation is affected by worldwide currents and weather systems, local factors, and even by various microstructures. When a region is heavily influenced by microstructure, a stochastic modeling approach may be appropriate.

The surface of the sea can generally be treated as a horizontal, near-perfect, reflector. Far more complex, the seabed is a lossy boundary that may have abrupt changes in material properties and topography. This is the more difficult boundary to deal with and must be carefully considered; the seafloor and underlying rock can have a strong influence on sound propagation. These layers can support a variety of waves, including compressional, shear, and interface waves, while the water only supports compressional wave propagation. The sea surface may not always be simple: ice cover in Arctic regions has a profound effect on sound propagation, and large waves on the open ocean incorporate enough air, in the form of bubbles, into the upper layer to have a marked affect on the sound speed. Similarly, gas released from the seafloor may affect the sound speed throughout the water column. The seafloor may have multiple layers of sediment atop a harder rock layer with stratifications dependent on geologic deposition, in the distant or not so distant past. The seafloor is mostly flat, with slopes rarely exceeding 10 degrees, but generally less than 5 degrees [2]. The structure of the seafloor, and its interactions with sound waves may be disregarded in some cases (long range, high frequency, deep water), but is paramount in others.

The distortion of sound waves, a result of many lossy interactions, is measured by a loss in signal strength over distance, the transmission loss

$$\mathrm{TL} = -20 \log_{10} \frac{|p(r,z)|}{|p_0|}$$

where $p(r,z)$ is the acoustic pressure at any point in the waveguide and p_0 is the pressure at the source. The main contributing factors to transmission loss are geometric spreading loss and absorption. Reflection and scattering losses also contribute to the total loss. Sound propagation in deep water is characterized by an upward refracting sound speed profile, permitting long-range propagation with negligible bottom interaction. The only mechanism affecting sound propagation in the deep sound channel is geometric spreading, allowing

acoustic signals to be recorded at distances as great as half way around the world. In the deep ocean with cold surface water, sound waves emitted from a source near the surface may refract downward at first, then reappear at the ocean surface at intervals with width on the order of ten kilometers. This so called convergence zone propagation can deliver high intensity signals to distant receivers near the surface with little distortion, and is typical of the North Atlantic. Deep oceans may have regions of turbulent surface activity that creates an isothermal layer near the surface. This surface duct acts as a waveguide, but can be quite lossy due to surface scattering. In shallow waters, sound tends to refract downward, as temperature decreases. Sound propagation in shallow water is dominated by lossy seafloor reflections and scattering losses. Bottom interaction, along with other factors including a high degree of parameter variability with range and time, makes long range predictions of sound propagation difficult. An optimal transmission frequency exists in most waveguides, and is heavily dependent on water depth.

A typical simplification to sound propagation problems is to assume most physical parameters do not vary with range. This may lead to fairly accurate results, but most parameters do vary with range, so models that can account for range dependence are fundamentally important. A common way to treat range dependence is to split the problem into range independent regions, then enforce certain continuity conditions on the boundary between each region. If the problem can be solved by a range-marching solution, environmental parameters may be updated at every range step, allowing for significant range dependence.

An acoustic model that accounts for various geological properties of the seafloor is a geoacoustic model. The seafloor has dramatic effects on sound waves interacting with it. Elastic media such as the rock making up the seafloor and ocean basement support both shear and compressional waves that must be accounted for. Sediment layers atop the ocean basement may take on a wide range of properties. An important consideration historically has been on approximating the elastic sediment bottom as a fluid, and on when this will

provide accurate results. When several layers of sediment sit on the seafloor, the seafloor may be reasonably treated as a fluid layer. Sediment layers are less rigid than rock and thus have a lower shear speed, sometimes sufficiently low enough that effects due to elasticity may be ignored without dramatic accuracy losses. Such a sediment may be called a transitional solid sediment. Some ypical sediments such as sands, silts, and clays have very low shear speeds and can thus be accurately treated as a fluid. If there is little or no sediment on the seafloor, the elasticity of the seafloor has a non-negligible effect on sound propagation in both the water and within the solid seafloor. The ocean basement attenuates sound and is thus lossy. The depth to which properties of the seafloor must be known is dependent on the frequency of the signal, as low frequency waves can travel much further into the seafloor than high frequency signals. Compressional wave speed, shear wave speed, their respective attenuations, and material density must all be accounted for by the geoacoustic model. All of these properties are depth dependent and may be difficult to measure in real world experiments. Since the geoacoustic properties of the seafloor vary greatly with location, geoacoustic models are location dependent and may yield very accurate predictions of sound propagation given accurate parameter inputs.

Reflectivity coefficients are an important measure of the effect on sound propagation by interactions at the fluid-sediment and sediment-basement interfaces. These coefficients can be used to account for bottom and reflection loss. The pressure reflection coefficient for an arbitrary fluid-solid layering may be constructed by repeated applications of the single-layer coefficient. This leads to recursive formulas that may be solved numerically, and are commonly found in ray models.

Sound propagation may be quantitatively predicted using sound propagation models. Based on the wave equation, propagation models use boundary conditions to describe the ocean environment. Certain interface conditions must be satisfied for stratified environments, as in the water-sediment-basement environment that this thesis focuses on. There are many

types of sound propagation models, of particular interest are fast field program (FFP), normal mode (NM), ray, parabolic equation (PE) models, and direct finite difference (FD) or finite element (FE) solutions to the full wave equation. All of these solutions allow for depth dependence; FFP and NM models cannot account for range dependence without modifications.

The parabolic equation method is useful for problems in several branches of mathematical physics, including underwater acoustics. Leontovich and Fock first applied a PE method while examining atmospheric radio wave propagation in the mid-1940s [1]. Parabolic equations can be derived for fluid media and a variety of elastic media types. The PE method is perhaps the most useful tool in modeling sound propagation in the ocean environment, and is based on parabolic approximations of the elliptic Helmholtz equation. It is more computationally efficient than FD/FE methods and can handle range dependence better than any other method mentioned above. The first application of PE solutions to ocean acoustics was in the early 1970's by Hardin and Tappert. Their application used a numerical solution based on fast Fourier transforms and has since become the most popular technique for solving range dependent problems. The parabolic equation method is an efficient and accurate theoretical tool for calculating the sound field at any receiver position [1].

The thrust of this thesis is to accurately treat a transitional solid sediment layer in a geoacoustic model. In addition to models that treat the entire propagation environment as a fluid, and models that treat the sediment layer as an elastic solid, models that treat the sediment as a porous elastic solid exist. A model that allows for fluid layers of differing density and sound speed beneath the water layer and overlying elastic basement layers could more accurately predict sound interaction with the seafloor in the presence of transitional solid sediments. Such a model is a helpful addition to the ocean acoustics community as it contributes to their ability to accurately model sound propagation in any ocean environment. The addition of a single non-water fluid layer between water and elastic bottom is

presented here, with concepts and methods that could be extended to a more complex propagation environment. In Chapter 2, the mathematical basis for two geoacoustic models of interest is presented. In Chapter 3, the particular mathematical problem encountered when introducing new layers is presented and possible solutions are discussed. In Chapter 4, implementation details, results, and an application of the improved model are given. Conclusions and suggestions for future work are given in Chapter 5.

CHAPTER 2

BACKGROUND

Parabolic equations in the context of acoustics problems may be derived for a variety of material types, including fluids, elastic and porous elastic solids, and atmospheric gases. Derivations of these equations often involve assumptions about the distance from the acoustic source to a point of interest and the relative strength of outgoing waves to the resulting incoming waves. Parabolic equations for fluid media are based on the acoustic wave equation

$$\rho \nabla \cdot \frac{1}{\rho} \nabla \tilde{p} - \frac{1}{c^2} \frac{\partial^2 \tilde{p}}{\partial t^2} = f \tag{2.1}$$

where ρ is the fluid density, $\tilde{p}$ is the acoustic pressure, c is the sound speed, f is a source function, and $\nabla = \langle \frac{\partial}{\partial x}, \frac{\partial}{\partial y}, \frac{\partial}{\partial z} \rangle$. In general, ρ, $\tilde{p}$, c, and f may vary with all three spatial coordinates and time t [1].

2.1 Fluid Parabolic Equation

Consider a fluid with density ρ that varies smoothly with depth. Assuming (2.1) has a separable, azimuthally symmetric solution $\tilde{p}(r, z, t) = p(r, z)e^{-i\omega t}$ about a time-harmonic source with frequency ω, the complex pressure p satisfies the Helmholtz equation

$$\frac{\partial^2 p}{\partial r^2} + \frac{1}{r} \frac{\partial p}{\partial r} + \rho \frac{\partial}{\partial z} \left(\frac{1}{\rho} \frac{\partial p}{\partial z} \right) + k^2 p = 0 \tag{2.2}$$

away from the source where $f = 0$. The wavenumber $k = \omega / c$ may vary in both range and depth as c may vary throughout the environment. Making the farfield assumption, $kr \gg 1$: that representative wavelengths $2\pi/k$ are much smaller than ranges of interest, we obtain

$$\frac{\partial^2 p}{\partial r^2} + \rho \frac{\partial}{\partial z} \left(\frac{1}{\rho} \frac{\partial p}{\partial z} \right) + k^2 p = 0.$$

This equation may be factored [1] as

$$\left(\frac{\partial}{\partial r} + ik_0\sqrt{1+Z}\right)\left(\frac{\partial}{\partial r} - ik_0\sqrt{1+Z}\right)p - \left(\frac{\partial}{\partial r}ik_0\sqrt{1+Z} - ik_0\sqrt{1+Z}\frac{\partial}{\partial r}\right)p = 0,$$

where k_0 is the representative or background wavenumber and depth operator Z is given by

$$Z = k_0^{-2}\left(\rho\frac{\partial}{\partial z}\left(\frac{1}{\rho}\frac{\partial}{\partial z}\right) + k^2 - k_0^2\right).$$

Assuming the environment does not vary with range, the operators $\frac{\partial}{\partial r}$ and $ik_0\sqrt{1+Z}$ commute yielding

$$\left(\frac{\partial}{\partial r} + ik_0\sqrt{1+Z}\right)\left(\frac{\partial}{\partial r} - ik_0\sqrt{1+Z}\right)p = 0.$$

Assuming outgoing energy dominates backscattered energy, we obtain the outgoing, parabolic wave equation,

$$\frac{\partial p}{\partial r} = ik_0\sqrt{1+Z}\,p. \tag{2.3}$$

To obtain an accurate and efficiently computed approximation to solution p, consider the formal solution to (2.3)

$$p(r+\Delta r, z) = e^{ik_0\Delta r\sqrt{1+Z}}p(r,z),$$

where Δr is the range step (see Appendix A for an explanation). This solution gives the pressure at depth at any range, provided an initial pressure and is thus called a range-marching scheme. Applying an n-term rational approximation to the exponential square root operator yields

$$p(r+\Delta r, z) \approx e^{ik_0\Delta r}\left(\prod_{j=1}^{n}\frac{1+\alpha_{j,n}Z}{1+\beta_{j,n}Z}\right)p(r,z)$$

where the complex coefficients $\alpha_{j,n}$ and $\beta_{j,n}$ are determined by placing accuracy and stability constraints on the Padé approximation [3]. A slightly modified version (discussed in Section 2.3) of this range-marching scheme is implemented in version 1.5 of the Range-Dependent Acoustic Model (RAM) developed by M. Collins at the Naval Research Laboratory [4]. RAM has been extensively tested against many known environments from a naval database. Many optimizations and advanced features were added at the Navy's request, culminating in the robust and capable Naval Standard Parabolic Equation Model used in both Naval research and fleet operations [5].

To obtain an initial field for the range-marching scheme, model a point source at $(r, z) = (0, z_0)$ by putting a forcing term on the right side of (2.2):

$$\frac{\partial^2 p}{\partial r^2} + \frac{1}{r}\frac{\partial p}{\partial r} + \rho \frac{\partial}{\partial z}\left(\frac{1}{\rho}\frac{\partial p}{\partial z}\right) + k^2 p = \frac{-2}{r}\delta(r)\delta(z - z_0), \tag{2.4}$$

where δ is the Dirac delta function. A self-starter, which gives the initial field based on environmental and source parameters, has been derived based on this equation. The approximate self-starter

$$p(r, z) = \sqrt{\frac{2\pi i}{r k_0}}(1 + Z)^{\frac{7}{4}} e^{i k_0 r \sqrt{1+Z}} \xi(z)$$

where $\xi(z)$ is a delta function smoothed to avoid numerical instabilities:

$$\xi(z) = \frac{\delta(z - z_0)}{(1 + Z)^2}$$

is evaluated at the first range step Δr, and is approximated for computational efficiency using a Padé expansion. Details are given in [3].

2.2 Elastic Parabolic Equation

Parabolic equations for elastic media are much more complicated than for fluid media, but have been formulated and implemented [6]. Consider an ocean environment with az-

imuthal symmetry about a point acoustic source. Scaling the unknown radial and vertical displacements U and W as $u = \sqrt{r}U$ and $w = \sqrt{r}W$ to account for cylindrical spreading [3], and assuming that representative wavelengths are much smaller than distances of interest from the source, the following equations of elastic motion are valid in range-independent environments:

$$\mu\frac{\partial^2 u}{\partial r^2} + \mu\frac{\partial^2 u}{\partial z^2} + \rho\omega^2 u + (\lambda+\mu)\frac{\partial \Delta}{\partial r} + \frac{\partial \mu}{\partial z}\frac{\partial u}{\partial z} + \frac{\partial \mu}{\partial z}\frac{\partial w}{\partial r} = 0 \tag{2.5}$$

and

$$\mu\frac{\partial^2 w}{\partial r^2} + \mu\frac{\partial^2 w}{\partial z^2} + \rho\omega^2 w + (\lambda+\mu)\frac{\partial \Delta}{\partial z} + 2\frac{\partial \mu}{\partial z}\frac{\partial w}{\partial z} + \frac{\partial \lambda}{\partial z}\Delta = 0. \tag{2.6}$$

Here, ω is the angular frequency of the source and $\Delta = \frac{\partial u}{\partial r} + \frac{\partial w}{\partial z}$ is the dilatation. Lamé moduli μ and λ are related to the shear and compressional wave speeds and density ρ, and thus can vary with depth (and range in range-dependent environments) [6]. The equations of motion (2.5) and (2.6) are also valid in fluids, where μ vanishes. Once Δ is obtained for a particular range, acoustic pressure may be calculated as $p(r,z) = \lambda(z)\Delta(z)$ in a fluid and $p(r,z) = \rho(z)c_b^2(z)\Delta(z)$ in a solid with shear speed c_b [6][7]. Differentiating (2.5) with respect to r and (2.6) with respect to z, and summing yields:

$$\begin{gathered}(\lambda+2\mu)\left(\frac{\partial^2 \Delta}{\partial r^2} + \frac{\partial^2 \Delta}{\partial z^2}\right) + \rho\omega^2\Delta + 2\frac{\partial \mu}{\partial z}\frac{\partial^2 w}{\partial r^2} + \omega^2\frac{\partial \rho}{\partial z}w + \\ \left(\frac{\partial \lambda}{\partial z} + 2\frac{\partial \mu}{\partial z}\right)\frac{\partial \Delta}{\partial z} + \frac{\partial}{\partial z}\left(\frac{\partial \lambda}{\partial z}\Delta\right) + 2\frac{\partial}{\partial z}\left(\frac{\partial \mu}{\partial z}\frac{\partial w}{\partial z}\right) = 0\end{gathered}. \tag{2.7}$$

The dependence on u is now entirely represented in the dependence on Δ in (2.7) and (2.6). Together they form the coupled system:

$$\frac{\partial^2}{\partial r^2} L\begin{pmatrix}\Delta \\ w\end{pmatrix} + M\begin{pmatrix}\Delta \\ w\end{pmatrix} = 0 \tag{2.8}$$

where

$$L = \begin{bmatrix}\lambda+2\mu & 2\frac{\partial \mu}{\partial z} \\ 0 & \mu\end{bmatrix}$$

and

$$M = \begin{bmatrix} M_{\Delta\Delta} & M_{\Delta w} \\ M_{w\Delta} & M_{ww} \end{bmatrix}$$

with

$$M_{\Delta\Delta}\Delta = (\lambda + 2\mu)\frac{\partial^2 \Delta}{\partial z^2} + \rho\omega^2\Delta + \left(\frac{\partial \lambda}{\partial z} + 2\frac{\partial \mu}{\partial z}\right)\frac{\partial \Delta}{\partial z} + \frac{\partial}{\partial z}\left(\frac{\partial \lambda}{\partial z}\Delta\right)$$

$$M_{\Delta w}w = \omega^2\frac{\partial \rho}{\partial z}w + 2\frac{\partial}{\partial z}\left(\frac{\partial \mu}{\partial z}\frac{\partial w}{\partial z}\right)$$

$$M_{w\Delta}\Delta = (\lambda + \mu)\frac{\partial \Delta}{\partial z} + \frac{\partial \lambda}{\partial z}\Delta$$

$$M_{ww}w = \mu\frac{\partial^2 w}{\partial z^2} + \rho\omega^2 w + 2\frac{\partial \mu}{\partial z}\frac{\partial w}{\partial z}.$$

The system is readily factorable as first derivatives with respect to r only appear within Δ. As in the fluid case, we may factor (2.8) to obtain the outgoing wave equation

$$\frac{\partial}{\partial r}\begin{pmatrix}\Delta \\ w\end{pmatrix} = ik_0\sqrt{I + \frac{L^{-1}(M - k_0^2 I)}{k_0^2}}\begin{pmatrix}\Delta \\ w\end{pmatrix} \tag{2.9}$$

where $k_0 = \omega/c_0$ for representative wave speed c_0 and I is the identity matrix.

An approximate solution $\binom{\Delta}{w}$ may be obtained by first writing the formal solution:

$$\left.\begin{pmatrix}\Delta \\ w\end{pmatrix}\right|_{r+\Delta r} = e^{ik_0\Delta r\sqrt{I+Z}}\left.\begin{pmatrix}\Delta \\ w\end{pmatrix}\right|_{r}$$

where depth operator

$$Z = \frac{1}{k_0^2}(L^{-1}M - k_0^2 I).$$

(see Appendix A for an explanation, note that the formula given therein apples to each scalar component of a vector equation). Applying a Padé approximation to the exponential square root operator yields:

$$\left.\begin{pmatrix}\Delta\\ w\end{pmatrix}\right|_{r+\Delta r} \approx e^{ik_0\Delta r}\prod_{j=1}^{n}\frac{I+a_{j,n}Z}{I+b_{j,n}Z}\left.\begin{pmatrix}\Delta\\ w\end{pmatrix}\right|_{r} \tag{2.10}$$

where n is the number of terms in the Padé series and $a_{j,n}$ and $b_{j,n}$ are complex Padé coefficients [3]. These complex coefficients are dependent on the number of Padé terms in the approximation, the entries of L and M, and accuracy and stability conditions. The coefficients are found by solving a linear system that arises from the definition of a Padé approximation [3].

Matrix inversion in the approximation (2.10) may be computed using the equivalent form

$$\left.\begin{pmatrix}\Delta\\ w\end{pmatrix}\right|_{r+\Delta r} \approx e^{ik_0\Delta r}\prod_{j=1}^{n}\frac{L+a_{j,n}LZ}{L+b_{j,n}LZ}\left.\begin{pmatrix}\Delta\\ w\end{pmatrix}\right|_{r}. \tag{2.11}$$

To see how operator division and the repeated product in (2.11) should be understood, let $n = 2$, yielding

$$\left.\begin{pmatrix}\Delta\\ w\end{pmatrix}\right|_{r+\Delta r} \approx e^{ik_0\Delta r}(L+b_{2,n}LZ)^{-1}(L+a_{2,n}LZ)(L+b_{1,n}LZ)^{-1}(L+a_{1,n}LZ)\left.\begin{pmatrix}\Delta\\ w\end{pmatrix}\right|_{r}. \tag{2.12}$$

In numerical implementations, operator matrices L and M are discretized, and (2.12) may be calculated by repeatedly solving linear systems using an elimination scheme (avoiding matrix inversion) similar to the elimination scheme described in Section 2.4 [1].

The starting field based on the point source is calculated in the same manner as in the fluid case [3], with self-starter

$$\begin{pmatrix}\Delta\\ w\end{pmatrix} = \sqrt{\frac{2\pi i}{k_0 r}}(I+Z)^{7/4}e^{ik_0\Delta r\sqrt{I+Z}}\begin{pmatrix}\frac{\delta(z-z_0)}{(I+Z)^2}\\ 0\end{pmatrix}.$$

The approximate solution is obtained by evaluating the self-starter at $r = \Delta r$ then marching the solution with (2.11).

2.3 Fluid-Elastic Parabolic Equation

The PE's main advantage over the Helmholtz equation is that the PE only solves for the outgoing part of the wave (this becomes a disadvantage in heavily range-dependent environments where backscattered energy in non-negligible); additionally it may be solved by a range-marching technique. The ocean surface is typically treated as a simple pressure release boundary requiring the easily implemented condition $p(r, 0) = 0$. The sea surface must be treated differently in the presence of ice cover or surface waves that incorporate a significant quantity of air into the water near the surface [1]. The lower boundary is more complicated; continuity conditions must be satisfied. In reality, the underlying elastic basement extends for thousands of kilometers, mathematically it is assumed to extend to infinity but in numerical implementations an absorbing layer several wavelengths thick is placed below the region of interest to prevent any artificial energy reflection.

At the interface between each layer of the stratified propagation environment, typically water overlying sediment layers atop elastic rock layers, certain conditions need to be satisfied. Between fluid layers, two conditions need to be satisfied:

$$p_a = p_b \tag{2.13}$$

and

$$\frac{1}{\rho_a}\frac{\partial p_a}{\partial z} = \frac{1}{\rho_b}\frac{\partial p_b}{\partial z} \tag{2.14}$$

where a and b denote respective fluid layers. These conditions correspond to continuity of complex pressure p and particle velocity across the interface. The conditions are satisfied in RAM which allows for multiple fluid layers with both smooth and discontinuous densities and sound speeds. Between a fluid and an elastic solid layer, three conditions must be satisfied:

$$\lambda_f \frac{\partial \Delta_f}{\partial z} + \rho_f \omega^2 w_b = 0, \tag{2.15}$$

$$\lambda_f \Delta_f = \lambda_b \Delta_b + 2\mu_b \frac{\partial w_b}{\partial z}, \tag{2.16}$$

and

$$\lambda_b \frac{\partial \Delta_b}{\partial z} + 2\mu \frac{\partial^2 w_b}{\partial z^2} + \rho_b \omega^2 w_b = 0 \tag{2.17}$$

where f denotes the fluid layer and b denotes the elastic solid layer. These conditions correspond to the continuity of vertical displacement, normal stress, and tangential stress. The implementation of the Range-Dependent Seismo-Acoustic Model (RAMS) by Collins explicitly enforces the fluid-solid interface conditions [6]. Implementation details are discussed in Section 3.3.

2.4 Numerical Implementations

Numerical solution techniques of the outgoing wave equation are widely variable; some techniques are particularly suited for specific acoustic environments. The split-step Fourier technique and various finite difference/finite element (FD/FE) techniques are widely used in the underwater acoustics community, although the split-step Padé solution is the most accurate and efficient. The Fourier technique is only computationally efficient for problems with negligible bottom interaction. Finite difference and finite element methods are well suited for bottom interacting problems of short range and frequencies lower than 200 Hz, giving solutions that are accurate for large angles from horizontal. Finite element methods more readily allow for variable vertical mesh spacing, which is useful for analyzing propagation involving a sloping interface, but uniform mesh FD methods are popular due to their simplicity. The split-step Padé solution devised by Collins has performed much faster than other FD/FE solutions, with comparable accuracy [1].

Energy conservation is a fundamental problem when applying the PE method to water columns with a sloping bottom interface that is approximated by piecewise horizontal stair-

steps. Energy is lost during upslope propagation and gained during downslope propagation. These errors are caused by poor assumptions in regards to the stair-step approximation of sloping interfaces, and may be eliminated by matching density-reduced pressure or using coordinate transformations in place of the stair-step approximation. Collins uses a modified depth operator $\widetilde{Z} = k_0^{-2}\left(\rho\frac{\partial}{\partial z}\frac{1}{\rho}\frac{\partial}{\partial z}\sqrt{\frac{\rho}{k}} + k^2 - k_0^2\right)$ and scaled pressure $p\sqrt{\frac{k}{\rho}}$ for energy conservation in his implementation of RAM, details may be found in [4].

The numerical solution of the fluid parabolic wave equation requires solving tridiagonal linear systems repeatedly, whereas the elastic PE solution involves heptadiagonal linear systems. The number of bands is related to the number of interface conditions. These systems correspond to discretized terms in the rational Padé approximation for a particular range step. More terms in the Padé approximation give wider angle solutions. These systems may be solved efficiently using a special elimination scheme (eliminates entries below main diagonal above the interface and above main diagonal below the interface) for problems involving variable ocean depth, a process that may be parallelized for additional efficiency. As the solution is marched in range, the matrices are updated to reflect changing environmental parameters. In RAMS, the entries of discretized L and M operator matrices from Section 2.2 are explicitly specified, then used to compute the matrices $L+b_{j,n}LZ$ and $L+a_{j,n}LZ$ that appear when (2.11) is discretized. For each range step, the n resulting linear systems are then solved, yielding an approximate sound field for the entire environment, which is then visualized by calculating transmission loss. Appropriate grid spacing may be determined by performing convergence tests (confirming that the solution does not vary for small changes in grid spacings) over range and depth steps, and the number of Padé terms used [4].

CHAPTER 3

ENFORCING INTERFACE CONDITIONS

The focus of this thesis is on modifying an existing elastic PE solution to allow for a transitional solid layer atop the seabed. A typical stratified ocean environment is shown in 3.1. Note that this environment is not shown to scale, the slope of the interface is steeper than typical in the ocean at about 15 degrees and is not suitable for applications of the parabolic equation technique. Interface conditions (2.13) to (2.17) need to be enforced at the appropriate interfaces.

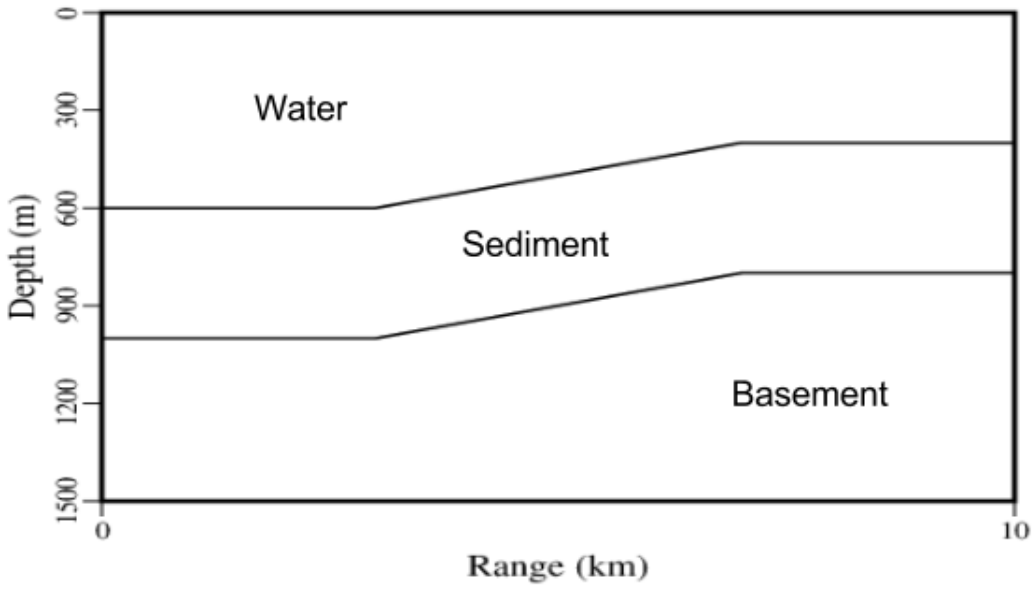

Figure 3.1: A stratified ocean environment

3.1 A Motivating Example

Consider the following piecewise defined boundary value problem:

$$\frac{d^2u}{dx^2} = f(x) = \begin{cases} 2, & x \in [0, s) \\ -2, & x \in [s, 2] \end{cases} \qquad u(0) = u(2) = 0, \tag{3.1}$$

subject to the conditions $u^{(a)} = u^{(b)}$ and $\alpha \frac{d}{dx} u^{(a)} = \beta \frac{d}{dx} u^{(b)}$ at the interface $x = s$, where $u^{(a)}$ and $u^{(b)}$ are the two pieces of the piecewise solution

$$u(x) = \begin{cases} u^{(a)}, & x \in [0, s] \\ u^{(b)}, & x \in [s, 2] \end{cases}$$

and α, β, and s are real constants. Integrate twice in each interval and apply interface conditions to get the piecewise solution

$$u(x) = \begin{cases} u^{(a)} = x^2 - \frac{-2(2\beta - 2\alpha s - 2\beta s + \alpha s^2)}{-2\alpha + \alpha s - \beta s} x, & x \in [0, s] \\ u^{(b)} = -x^2 + \frac{4\alpha + 2\beta s^2}{2\alpha - \alpha s + \beta s} x - \frac{4(\alpha s - \beta s + \beta s^2)}{-2\alpha + \alpha s - \beta s}, & x \in [s, 2] \end{cases}$$

Let the interval $[0, 2]$ be split into $n - 1$ subintervals of equal length. An approximate solution $U_i := U(x_i) \approx u(x_i)$, $i = 0, ..., n - 1$, is sought on the n-element grid with uniform spacing $\Delta x = 2/(n - 1)$. The grid points are located at $x_i = i\Delta x$. Assume the interface $x = s$ lies between the two adjacent grid points x_{j-1} and x_j (not necessarily at the midpoint), for some index j. The boundary conditions fix $U_0 = U_{n-1} = 0$. This approximation will also be piecewise:

$$U_i = \begin{cases} u_i^{(a)} \approx u^{(a)}(x_i), & i = 1, ..., j - 1 \\ u_i^{(b)} \approx u^{(b)}(x_i), & i = j, ..., n - 2 \end{cases}$$

Applying the standard second order finite difference approximation to $\frac{d^2u}{dx^2}$ we obtain

$$\frac{U_{i-1} - 2U_i + U_{i+1}}{\Delta x^2} = f_i := f(x_i),\ i = 1, ..., j - 2,\ i = j + 1, ...n - 2, \tag{3.2}$$

which is valid throughout the interior of the domain, except at two points around the interface. At the $i = j - 1$ and $i = j$ steps, the difference relation reads, respectively,

$$\frac{u_{j-2}^{(a)} - 2u_{j-1}^{(a)} + u_j^{(a)}}{\Delta x^2} = f_{j-1} \tag{3.3}$$

and

$$\frac{u_{j-1}^{(b)} - 2u_j^{(b)} + u_{j+1}^{(b)}}{\Delta x^2} = f_j. \tag{3.4}$$

Each approximation contains what are termed nonphysical values: $u_j^{(a)}$ and $u_{j-1}^{(b)}$ do not exist in the piecewise definition of the problem domain. At this point, attempting to access these values is akin to attempting to access values just outside the end and beginning of a one-dimensional array on a computer. To account for these nonphysical values, we discretely approximate the interface conditions about the interface. To obtain an accurate approximation to the derivatives in the second interface condition, introduce x_* opposite the interface from the grid point nearest the interface, as shown in 3.2 for the case when the interface is closest to x_j at a distance of $\Delta x_2 = x_j - s$. Note that $\Delta x_1 = s - x_{j-1}$ and so $\Delta x_1 + \Delta x_2 = \Delta x$.

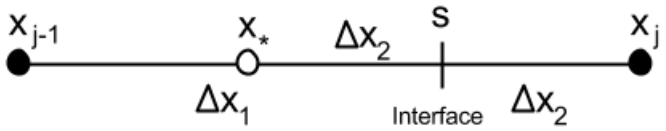

Figure 3.2: Introduction of x_*

Linearly interpolation gives good approximations for U at points between x_{j-1} and x_j:

$$U_s := U(s) = \frac{u_{j-1}\Delta x_2 + u_j \Delta x_1}{\Delta x}$$

and

$$U_* := U(x_*) = \frac{u_{j-1} 2\Delta x_2 + u_j(\Delta x_1 - \Delta x_2)}{\Delta x}.$$

With interpolated values at the interface, the first interface condition reads

$$\frac{u_{j-1}^{(a)} \Delta x_2 + u_j^{(a)} \Delta x_1}{\Delta x} = \frac{u_{j-1}^{(b)} \Delta x_2 + u_j^{(b)} \Delta x_1}{\Delta x}. \tag{3.5}$$

This relation holds regardless of which grid point the interface is closer to. Discretizing the second condition, centered at x_s gives

$$\alpha \frac{u_j^{(a)} - u_*^{(a)}}{2\Delta x_2} = \beta \frac{u_j^{(b)} - u_*^{(b)}}{2\Delta x_2}.$$

Inserting U_* yields

$$\alpha \frac{u_j^{(a)} - \frac{u_{j-1}^{(a)} 2\Delta x_2 + u_j^{(a)}(\Delta x_1 - \Delta x_2)}{\Delta x}}{2\Delta x_2} = \beta \frac{u_j^{(b)} - \frac{u_{j-1}^{(b)} 2\Delta x_2 + u_j^{(b)}(\Delta x_1 - \Delta x_2)}{\Delta x}}{2\Delta x_2}$$

which simplifies to

$$\beta \frac{u_j^{(a)} - u_{j-1}^{(a)}}{\Delta x} = \alpha \frac{u_j^{(b)} - u_{j-1}^{(b)}}{\Delta x}. \tag{3.6}$$

Notice this relation does not depend on Δx_1 or Δx_2: it holds regardless of where the interface is with respect to the surrounding grid points. This is a result of approximating U as linear on the subinterval $[x_{j-1}, x_j]$ to obtain the interpolated value U_*; under this approximation the rate of change in U is the same for any two points in the subinterval. The system of two equations (3.5) and (3.6) relates the two nonphysical values to physical values, solving the system gives

$$u_j^{(a)} = \frac{\beta \Delta x}{\beta \Delta x_1 + \alpha \Delta x_2} u_j^{(b)} + \frac{(\alpha - \beta)\Delta x_2}{\beta \Delta x_1 + \alpha \Delta x_2} u_{j-1}^{(a)}$$

and

$$u_{j-1}^{(b)} = \frac{(\beta-\alpha)\Delta x_1}{\beta\Delta x_1 + \alpha\Delta x_2} u_j^{(b)} + \frac{\alpha\Delta x}{\beta\Delta x_1 + \alpha\Delta x_2} u_{j-1}^{(a)}.$$

Inserting these relations into (3.3) and (3.4), we obtain

$$u_{j-2}^{(a)} + \left(\frac{(\alpha-\beta)\Delta x_2}{\beta\Delta x_1 + \alpha\Delta x_2} - 2 \right) u_{j-1}^{(a)} + \frac{\beta\Delta x}{\beta\Delta x_1 + \alpha\Delta x_2} u_j^{(b)} = \Delta x^2 f_{j-1} \tag{3.7}$$

and

$$\frac{\alpha\Delta x}{\beta\Delta x_1 + \alpha\Delta x_2} u_{j-1}^{(a)} + \left(\frac{(\beta-\alpha)\Delta x_1}{\beta\Delta x_1 + \alpha\Delta x_2} - 2 \right) u_j^{(b)} + u_{j+1}^{(b)} = \Delta x^2 f_j. \tag{3.8}$$

These equations and those of (3.2) form an $n-2 \times n-2$ dimensional linear system, which may be written as a tridiagonal linear system

$$\begin{bmatrix} -2 & 1 & & & & & & & \\ 1 & \ddots & \ddots & & & & 0 & & \\ & \ddots & -2 & 1 & & & & & \\ & & 1 & \left(\frac{(\alpha-\beta)\Delta x_2}{\beta\Delta x_1+\alpha\Delta x_2} - 2\right) & \frac{\beta\Delta x}{\beta\Delta x_1+\alpha\Delta x_2} & & & & \\ & & & \frac{\alpha\Delta x}{\beta\Delta x_1+\alpha\Delta x_2} & \left(\frac{(\beta-\alpha)\Delta x_1}{\beta\Delta x_1+\alpha\Delta x_2} - 2\right) & 1 & & & \\ & & & & 1 & -2 & \ddots & & \\ & & 0 & & & \ddots & \ddots & 1 & \\ & & & & & & 1 & -2 & \end{bmatrix} \begin{bmatrix} u_1^{(a)} \\ \vdots \\ u_{j-2}^{(a)} \\ u_{j-1}^{(a)} \\ u_j^{(b)} \\ u_{j+1}^{(b)} \\ \vdots \\ u_{n-2}^{(b)} \end{bmatrix} = \Delta x^2 \begin{bmatrix} f_1 \\ \vdots \\ f_{j-2} \\ f_{j-1} \\ f_j \\ f_{j+1} \\ \vdots \\ f_{n-2} \end{bmatrix}$$

that is easily solved on a computer. Solving the system yields an approximate solution with accuracy that increases with increasing n.

Suppose the interface lies instead *on* grid point x_{j-1}. The first interface condition allows us to consider this grid point to be in $[s, 2]$ without loss of generality. This choice changes the indexing of the approximate solution:

$$U_i = \begin{cases} U_i^{(a)} \approx u^{(a)}(x_i), & i = 1, ..., j-2 \\ U_i^{(b)} \approx u^{(b)}(x_i), & i = j-1, ..., n-2 \end{cases}$$

but yields the same nonphysical values. The formulas for the nonphysical values and the entries of the linear system remain the same, with $\Delta x_1 = 0$ and $\Delta x_2 = \Delta x$. An alternate approach to the case when the interface lies on a grid point is given in Appendix B. Both approaches yield similar maximum absolute error for a variety of n values, neither one is consistently more accurate.

The plots in 3.3 display the importance of enforcing the interface conditions. Approximate solutions are compared to exact solutions and naïve approximations to the solutions, where interface conditions are not enforced (the tridiagonal matrix has -2's along the main diagonal and 1's along the sub- and super-diagonals). Only the endpoints of the naïve approximations agree with the analytic solutions, and there is a large error in the interior of the domain, especially at the center. The error in the approximate solutions with interface conditions enforced are shown alongside the comparisons between approximate solutions and the exact solutions. The approximate solutions with interface conditions enforced agree very well with the exact solution when the interface lies at the midpoint of two grid points as shown in 3.3(a&b), when the interface lies on a grid points as shown in 3.3(c&d), and when the interface lies between grid points but not at the midpoint of those grid points as shown in 3.3(e&f). The parameters $\alpha = 1$ and $\beta = 2$ are the same in each plot, the interface is at $x = 1$ in 3.3(a to d) and at $x = 1.3$ in 3.3(e&f). The approximate solution is most accurate when the interface lies at the midpoint of two grid points (a result of interpolation), the error is greatest at the interface, and falls with increasing n in all three cases.

3.2 The Fluid-Fluid Interface

The coupled system (2.8) may be discretized according to the discrete depth operators specified in Appendix A of [6]. The computer program RAMS uses the discretization of (2.8) in (2.10) to approximate $\binom{\Delta}{w}$ and eventually calculates the complex pressure. The primary concern in adding a transitional solid sediment layer between the liquid water layer and

elastic seafloor layers is satisfying both fluid-fluid interface pressure conditions (2.13) and (2.14). The discretization of these conditions will give explicit formulae for the nonphysical-values that appear in the discretizations of (2.6) and (2.7) around the interface. Note that in RAMS, λ is assumed to be piecewise linear in depth at any range step. In fluid layers where the shear modulus μ vanishes, (2.6) and (2.7) become

$$\rho\omega^2 w + \lambda\frac{\partial\Delta}{\partial z} + \frac{\partial\lambda}{\partial z}\Delta = 0 \tag{3.9}$$

and

$$\lambda\frac{\partial^2\Delta}{\partial r^2} + \lambda\frac{\partial^2\Delta}{\partial z^2} + \rho\omega^2\Delta + \omega^2\frac{\partial\rho}{\partial z}w + 2\frac{\partial\lambda}{\partial z}\frac{\partial\Delta}{\partial z} = 0. \tag{3.10}$$

The equations of motion in a fluid, (3.9) and (3.10) may be written in the form (2.8) with

$$L = \begin{bmatrix} \lambda & 0 \\ 0 & 0 \end{bmatrix}$$

and

$$M_{\Delta\Delta}\Delta = \lambda\frac{\partial^2\Delta}{\partial z^2} + \rho\omega^2\Delta + 2\frac{\partial\lambda}{\partial z}\frac{\partial\Delta}{\partial z}$$

$$M_{\Delta w}w = \omega^2\frac{\partial\rho}{\partial z}w$$

$$M_{w\Delta}\Delta = \lambda\frac{\partial\Delta}{\partial z} + \frac{\partial\lambda}{\partial z}\Delta$$

$$M_{ww}w = \rho\omega^2 w.$$

For any range step, the vertical domain is divided into equally spaced subintervals of length Δz, with grid points indexed so that $z_i = i\Delta z$. Applying the Galerkin-inspired discrete depth operators listed in Appendix A of [6] to the simplified system gives

$$\lambda_{i+1}\Delta_{i+1} = \frac{\lambda_i + \lambda_{i+1}}{12}\Delta_i + \frac{\lambda_i + 6\lambda_{i+1} + \lambda_{i+2}}{12}\Delta_{i+1} + \frac{\lambda_{i+1} + \lambda_{i+2}}{12}\Delta_{i+2}, \tag{3.11}$$

$$M_{\Delta\Delta}\Delta_{i+1} = \left(\frac{\lambda_i}{\Delta z^2} + \omega^2\frac{\rho_i + \rho_{i+1}}{12}\right)\Delta_i + \left(\frac{-\lambda_i - \lambda_{i+2}}{\Delta z^2} + \omega^2\frac{\rho_i + 6\rho_{i+1} + \rho_{i+2}}{12}\right)\Delta_{i+1} + \left(\frac{\lambda_{i+2}}{\Delta z^2} + \omega^2\frac{\rho_{i+1} + \rho_{i+2}}{12}\right)\Delta_{i+2}, \tag{3.12}$$

$$M_{\Delta w}w_{i+1} = \omega^2\frac{-\rho_i + \rho_{i+1}}{6\Delta z}w_i + \omega^2\frac{-\rho_i + \rho_{i+2}}{3\Delta z}w_{i+1} + \omega^2\frac{-\rho_{i+1} + \rho_{i+2}}{6\Delta z}w_{i+2}, \tag{3.13}$$

$$M_{w\Delta}\Delta_{i+1} = \frac{-2\lambda_i - \lambda_{i+1}}{6\Delta z}\Delta_i + \frac{-\lambda_i + \lambda_{i+2}}{6\Delta z}\Delta_{i+1} + \frac{\lambda_{i+1} + 2\lambda_{i+2}}{6\Delta z}\Delta_{i+2}, \tag{3.14}$$

and

$$M_{ww}w_{i+1} = \omega^2\frac{\rho_i + \rho_{i+1}}{12}w_i + \omega^2\frac{\rho_i + 6\rho_{i+1} + \rho_{i+2}}{12}w_{i+1} + \omega^2\frac{\rho_{i+1} + \rho_{i+2}}{12}w_{i+2}. \tag{3.15}$$

These discretizations are valid in both fluid layers, except at two points around the interface. The pressure release boundary condition at $z = 0$ is enforced by setting $\Delta_0 = 0$. Unlike the discretizations used in RAMS, these updated discretizations allow for variable densities in fluid layers. The second derivative in range is dealt with in the parabolic approximation, as discussed in Section 2.2.

Let the fluid-fluid interface lie between grid points z_{j-1} and z_j, or on z_{j-1}, at any range step, with index j depending on the range step. Nonphysical values $\Delta_{j-1}^{(s)}$ and $\Delta_j^{(w)}$ appear in (3.11) to (3.15) for indices $i = j - 2$ and $i = j - 1$. Superscript (w) indicates a value in the water, superscript (s) indicates a value in the sediment. To find formulas for the nonphysical-values, use the same approach as in Section 3.1. Following the approach of Section 3.1, with $\alpha = \rho_s$ and $\beta = \rho_w$, we discretely approximate the interface conditions (2.13) and (2.14) (with the two fluid layers being the water and the sediment layers, denoted

now with superscripts) across the interface. This gives a system of two equations for two unknown, nonphysical pressure values $p_{j-1}^{(s)}$ and $p_j^{(w)}$:

$$\frac{p_{j-1}^{(w)}\Delta z_2 + p_j^{(w)}\Delta z_1}{\Delta z} = \frac{p_{j-1}^{(s)}\Delta z_2 + p_j^{(s)}\Delta z_1}{\Delta z}$$

and

$$\frac{1}{\rho_s}\frac{p_j^{(w)} - p_{j-1}^{(w)}}{\Delta z} = \frac{1}{\rho_w}\frac{p_j^{(s)} - p_{j-1}^{(s)}}{\Delta z}$$

where Δz_1 is the distance from z_{j-1} to the interface and Δz_2 is the distance from the interface to z_j. Solving this system of equations yields formulas for the nonphysical pressures, as linear combinations of the physical quantities $p_{j+1}^{(w)}$ and $p_{j+2}^{(s)}$:

$$p_j^{(w)} = \frac{\rho_w\Delta z}{\rho_w\Delta z_1 + \rho_s\Delta z_2}p_j^{(s)} + \frac{(\rho_s - \rho_w)\Delta z_2}{\rho_w\Delta z_1 + \rho_s\Delta z_2}p_{j-1}^{(w)}$$

and

$$p_{j-1}^{(s)} = \frac{(\rho_w - \rho_s)\Delta z_1}{\rho_w\Delta z_1 + \rho_s\Delta z_2}p_j^{(s)} + \frac{\rho_s\Delta z}{\rho_w\Delta z_1 + \rho_s\Delta z_2}p_{j-1}^{(w)}$$

These formulas may be rewritten as formulas for the nonphysical-values $\Delta_{j+1}^{(s)}$ and $\Delta_{j+2}^{(w)}$ in terms of physical values $\Delta_{j+1}^{(w)}$ and $\Delta_{j+2}^{(s)}$ using the relation $p = \lambda\Delta$ which holds in both fluid layers. The relation gives:

$$\Delta_j^{(w)} = \frac{\rho_w\Delta z}{\rho_w\Delta z_1 + \rho_s\Delta z_2}\frac{\lambda_j^{(s)}}{\lambda_j^{(w)}}\Delta_j^{(s)} + \frac{(\rho_s - \rho_w)\Delta z_2}{\rho_w\Delta z_1 + \rho_s\Delta z_2}\frac{\lambda_{j-1}^{(w)}}{\lambda_j^{(w)}}\Delta_{j-1}^{(w)}$$

and

$$\Delta_{j-1}^{(s)} = \frac{(\rho_w - \rho_s)\Delta z_1}{\rho_w\Delta z_1 + \rho_s\Delta z_2}\frac{\lambda_j^{(s)}}{\lambda_{j-1}^{(s)}}\Delta_j^{(s)} + \frac{\rho_s\Delta z}{\rho_w\Delta z_1 + \rho_s\Delta z_2}\frac{\lambda_{j-1}^{(w)}}{\lambda_{j-1}^{(s)}}\Delta_{j-1}^{(w)}$$

Substituting these formulas into (3.11) to (3.15) at the appropriate depth steps will make them consist of physical Δ values only, explicitly enforcing the interface conditions.

3.3 The Fluid-Solid Interface

Nonphysical values also appear in the discretization of (2.8) at the fluid-solid interface. The conditions (2.15), (2.16), and (2.17) must be satisfied at this interface. Finite difference formulas for the interface conditions give explicit formulas for the three nonphysical-values, $\Delta_{j+1}^{(w)}$, $\Delta_{j-1}^{(b)}$, and $v_{j-1}^{(b)}$ which appear when the interface lies between grid points z_{j-1} and z_j, or on z_{j-1}. The obtained formulas are used as corrections to matrix entries in RAMS in the same manner as discussed in Section 3.1 [6].

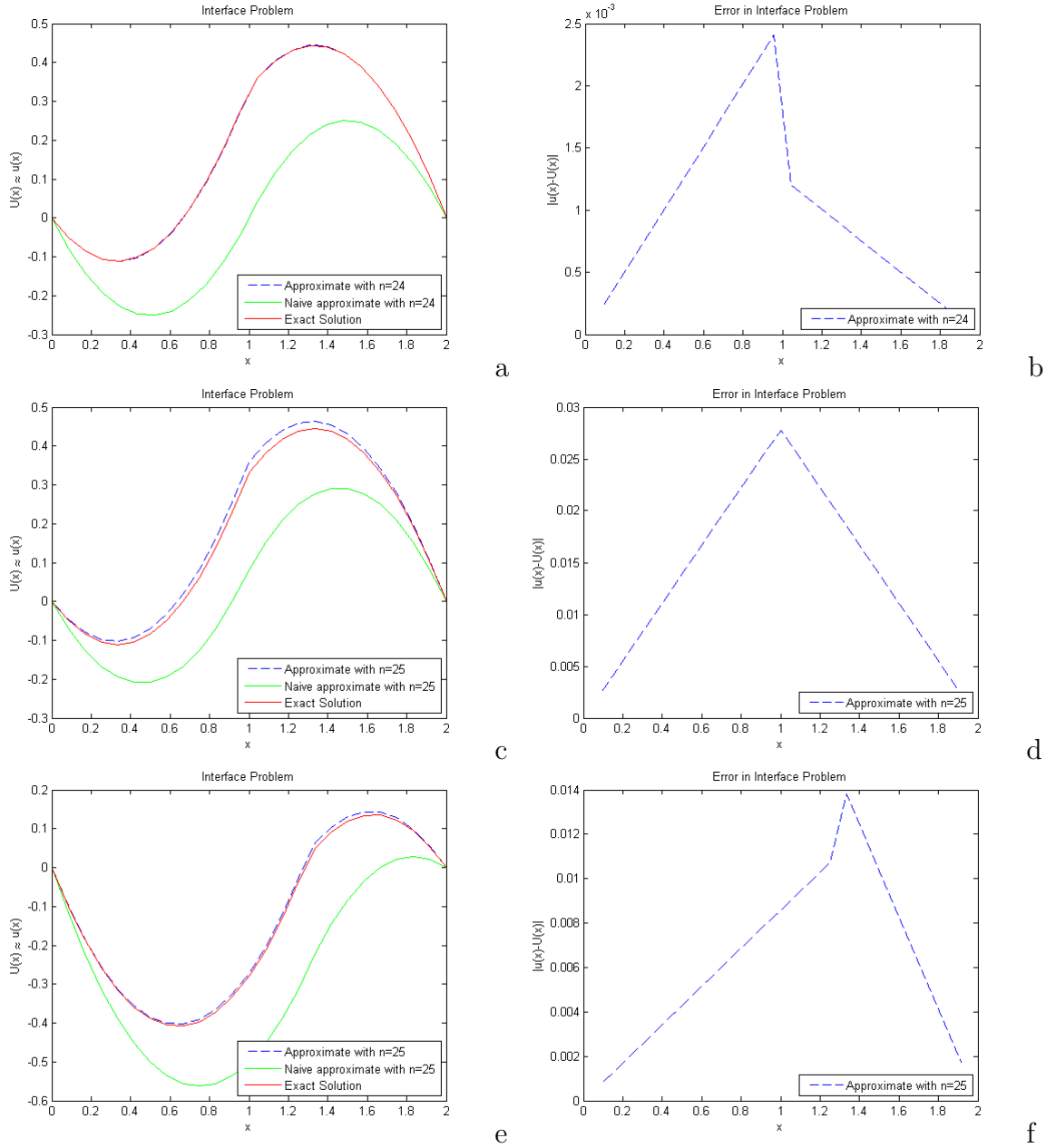

Figure 3.3: Approximate solutions to the interface condition problem when the interface a) is at the midpoint of the surrounding grid points, c) is on a grid point, and e) is between grid points but not at their midpoint. Error in approximate solutions: (b), (c), and (d).

CHAPTER 4

IMPLEMENTATION AND RESULTS

The aim of this thesis is to add a transitional solid sediment layer, modeled as a denser than water fluid, to the fluid-elastic PE model implementation that is RAMS. The program with added functionality has been named RAMX. RAMS approximates a solution to the elastic equations of motion (2.5) and (2.6), which are valid in both the water layer and the sediment layer, as described in Sections 2.2 to 2.4. To add the transitional solid sediment layer, RAMS was modified to use variable density and compressional wave speed values in distinct fluid layers. The fluid-fluid interface conditions are explicitly enforced at the appropriate depth steps.

4.1 Modification of RAMS

To account for a variable density fluid layer, RAMS needed to be modified in a few ways. In RAMS the density of the only fluid, water, is assumed to be 1.0 g/cm^3 and is implicitly present whenever it is part of a product in the discretizations of (2.5) and (2.6). These assumed density values had to be tracked down and replaced by a variable for density. In particular this change affected the fluid-solid interface conditions, the values of λ in the fluid, and the discretization of the equations of motion. Fluid density appears outside it's corresponding λ value in only one of the fluid-solid interface conditions,(2.15). Fluid density appears in the formula $\lambda = \rho c^2$ which is valid in fluid layers, and calculated in RAMS. Compressional wave speed c may depend on depth at any range step. The assumption of constant density allowed the $\omega^2 \frac{\partial \rho}{\partial z} w$ term in (3.10) to be dropped, and yielded simpler discretizations of the $\rho\omega^2 w$ terms in (3.9) and (3.10) in RAMS. To properly account for variable density all three terms were discretized according to the discrete depth operators

given in Appendix A of [6], yielding additional terms that are given in (3.12), (3.13), and (3.15).

The fluid-fluid interface is specified by a sediment thickness parameter: the interface parallels the fluid-solid interface which is specified separately. The entries of (3.11) to (3.15) are explicitly specified by RAMX at every depth step. When a discretization crosses the fluid-fluid interface, the entries are modified to account for nonphysical values, enforcing the interface conditions. The formulas for the nonphysical values were obtained under the assumption that the interface lies at the midpoint of two grid points, when the interface does not lie at the midpoint additional errors affect the approximation. The largest of these errors occur when the interface lies on a grid point, in this case RAMX perturbs the interface so that discretizations always cross the interface. The problem is entirely avoidable by adjusting the depth step size. This convention produces accurate results, but more accurate results could be obtained by accounting for the nonphysical values that appear. An introduction to enforcing interface conditions when the interface lies on a grid point is given in Appendix B. Density values that appear in the formulas for nonphysical-values are taken to have the same index as the center of the discretization that the nonphysical-value appears in. All density and sound speed values are considered physical, even if they fall outside the region they describe.

4.2 Added Functionality

RAMX has two main advantages over RAMS. Primarily, RAMX has an additional fluid layer that may have a distinctly different density and sound speed from the surrounding layers. This new layer approximates a sediment with low shear speed, while RAMS may be inaccurate for environments with low shear speed layers. Additionally, RAMX allows for a density profile in every layer, including the water layer. The addition of density variability in the water layer permits functionality not found in RAM or RAMX.

4.1(b) is showing an example that demonstrates all of the added functionality: all sound speed and density parameters increase with depth and are discontinuous at interfaces. The 30 Hz source is at 300.0 meters. The sediment layer is 300.5 meters thick and has a slope of about 1.43 degrees in the center of the environment. In the water, sound speed increases linearly from 1475.0 m/s to 1525.0 m/s and the density increases linearly from 1.0 g/cm^3 to 1.3 g/cm^3. In the sediment sound speed increases linearly from 1700.0 m/s to 1750.0 m/s and the density increases linearly from 1.5 g/cm^3 to 1.7 g/cm^3. This sediment has properties similar to that of sandy silt or silty sand [8]. In the elastic layer sound speed increases linearly from 1800.0 m/s to 1850.0 m/s, shear speed increases linearly from 400.0 m/s to 800.0 m/s and the density increases linearly from 2.0 g/cm^3 to 2.5 g/cm^3. 4.1(a) is a RAMS result with the same fluid-solid interface and solid layer, no sediment layer, sound speed increases linearly from 1475.0 m/s to 1525.0 m/s, and fixed density 1.0 g/cm^3.

This example demonstrates the additions to RAMS: variable sound speed and density in distinct fluid layers. The high density is water is very unrealistic, but may be considered an exaggeration of density anomalies that occur when surface waters from different sources mix, such as a fresh water river flowing into a salt water lake, or deviser waters of the Mediterranean Sea mixing with the Atlantic Ocean.

4.3 Verification of Functionality

To verify that RAMX is accurately modeling the fluid sediment, we compare it to RAM and RAMS for a few scenarios. The plots shown give transmission loss contours (color plots with color coded transmission loss, axes are range and depth) and curves (line plots with transmission loss at a particular depth, axes are range and transmission loss). Note that the color plots are not to scale, the environments they provide a view of are much wider.

RAMX and RAMS should compare exactly when the sediment parameters in RAMX match the water parameters in RAMS. We see this behavior in 4.2 where the speed of sound

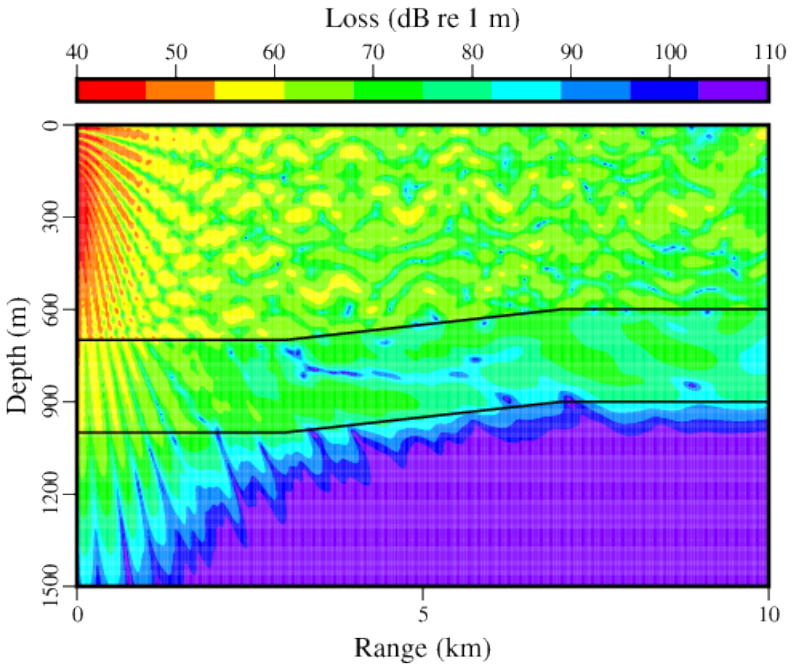

a

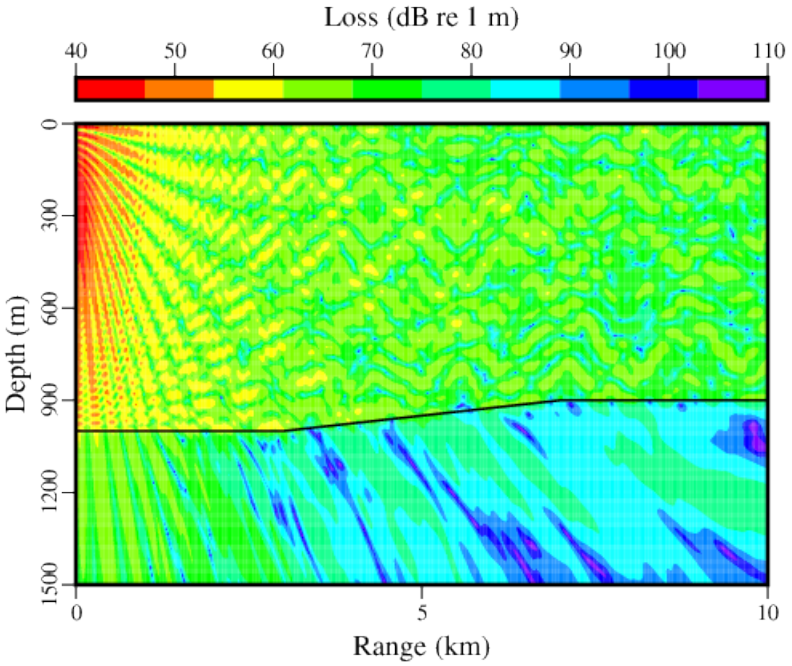

b

Figure 4.1: Transmission loss contours in a) RAMX with increasing and discontinuous environmental properties b) RAMS with fixed fluid density 1.0 g/cm^3 and no sediment

is 1500 m/s and the density is 1.0 g/cm^3 in all fluid layers. The frequency is 50.0 Hz, the source and receiver are at a depth of 100 meters, the water-basement interface has a slope of about 1.5 degrees and initial depth of 700.5 meters, the basement has compressional speed 1700.0 m/s, shear wave speed 400.0 m/s and density 1.1 g/cm^3, and there is an attenuating layer starting at depth 4000.0 meters. We see exact agreement between 4.2(a) and 4.2(b), more easily seen at a particular depth in 4.2(c). This comparison verifies the RAMX retains the functionality of RAMS, its predecessor.

RAMX and RAM should compare well when the sediment is thick enough to make bottom interaction negligible. Upward refracting sound speed profiles are selected to further reduce bottom interaction. We see this behavior for three distinct frequencies in 4.3: 25 Hz, 4.4: 70 Hz, and 4.5: 140 Hz. Similar results have been obtained for other frequencies: these results are representative. The sediment layer is 9500.5 meters thick. The seafloor has a slope of about 1.5 degrees In the water layer, which has initial depth 499.5 meters, the sound speed increases linearly with depth from 1475.0 m/s at the surface to 1525.0 m/s at 499.5 meters deep. The fluid sediment layer has density 1.3 g/cm^3 and sound speed that increases linearly with depth from 1700.0 m/s at the water-sediment interface to 1750.0 m/s at 4000.0 meters deep. This sediment has properties similar to that of silty clays, but is unrealistically thick [8].The source is at 300 meters and receiver is at 250 meters. RAMX and RAM have good agreement when the sediment layer is very thick, slight differences can be seen comparing subplots (a) and (b) of 4.3, 4.4, and 4.5 and at a particular depth in subplots (c) of 4.3, 4.4, and 4.5. These differences may be attributed to errors in enforcing the fluid-fluid interface conditions in RAMX: the interface does not generally lie at the midpoint of its surrounding grid points, an assumption made when finding formulas for the nonphysical-values.

Further, we expect RAMX with a fluid sediment to compare well with RAMS with an elastic sediment with low shear speed, we see this behavior for three distinct frequencies in 4.6: 25 Hz, 4.8: 50 Hz, and 4.10: 100 Hz. Similar results have been obtained for other

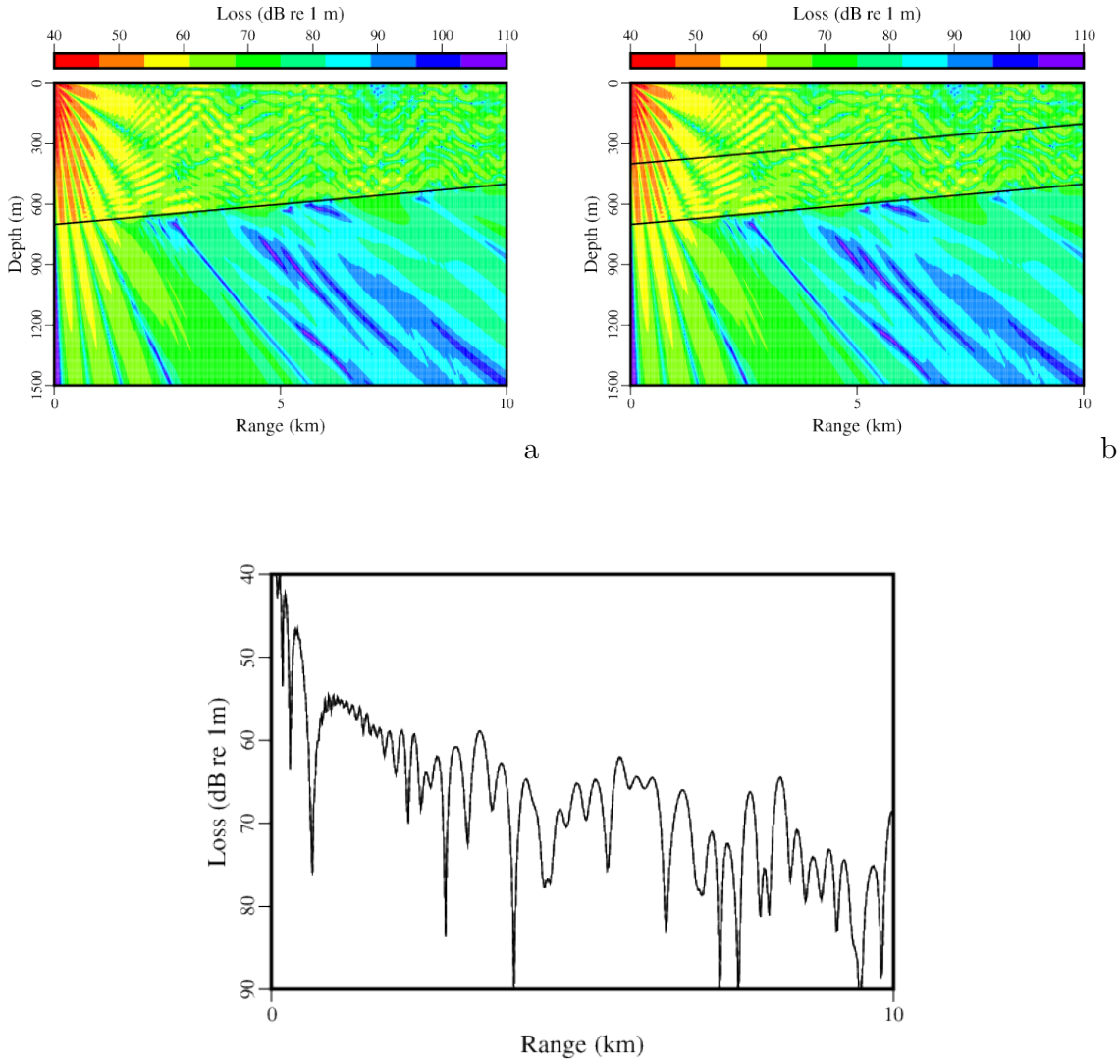

Figure 4.2: Transmission loss contours in RAMS and RAMX with water sediment. a) RAMS, b) RAMX, c) comparison at receiver depth 100 meters, the dashed curve is RAMX.

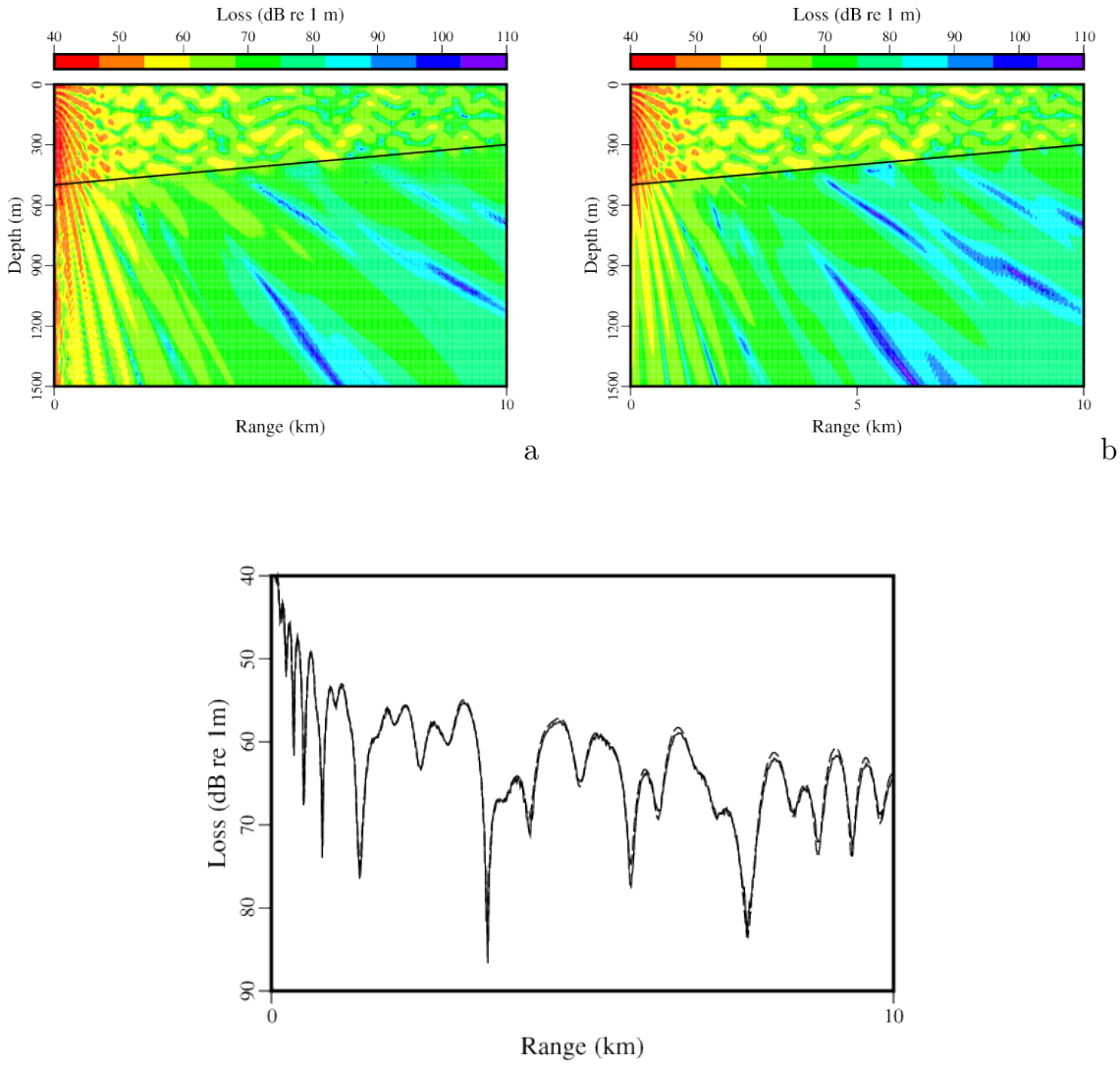

Figure 4.3: Transmission loss contours in RAM and RAMX with thick sediment for a frequency of 25 Hz. a) RAM, b)RAMX, c) comparison at receiver depth 250 meters: the dashed curve is RAMX.

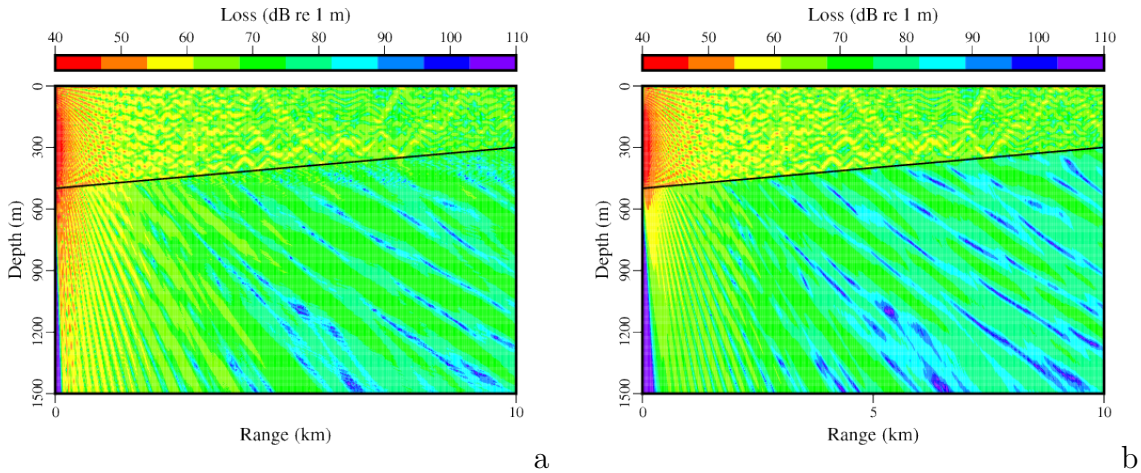

a b

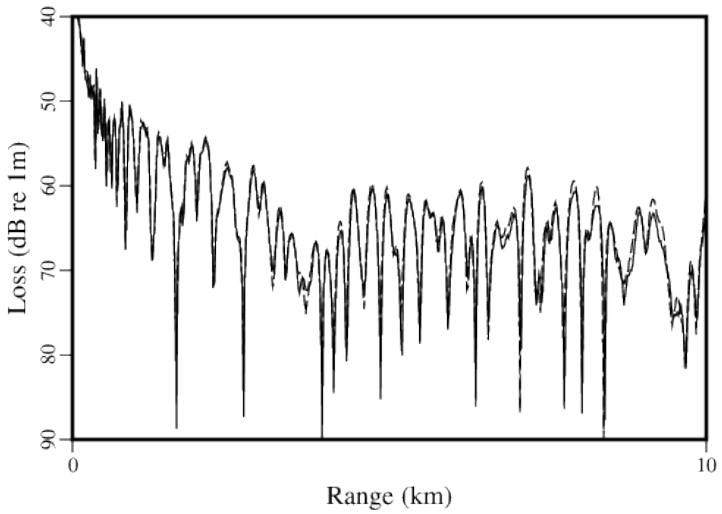

c

Figure 4.4: Transmission loss contours in RAM and RAMX with thick sediment for a frequency of 70 Hz. a) RAM, b)RAMX, c) comparison at receiver depth 250 meters: the dashed curve is RAMX.

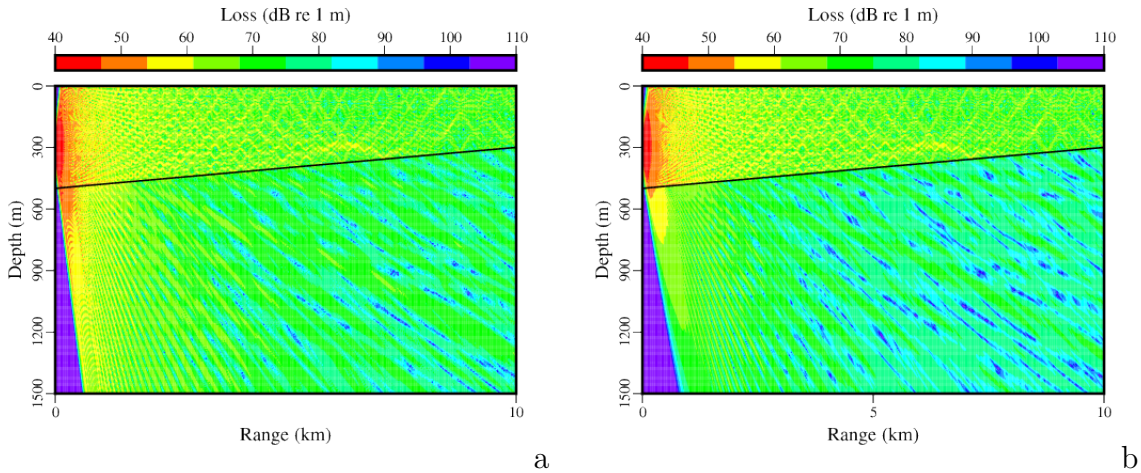

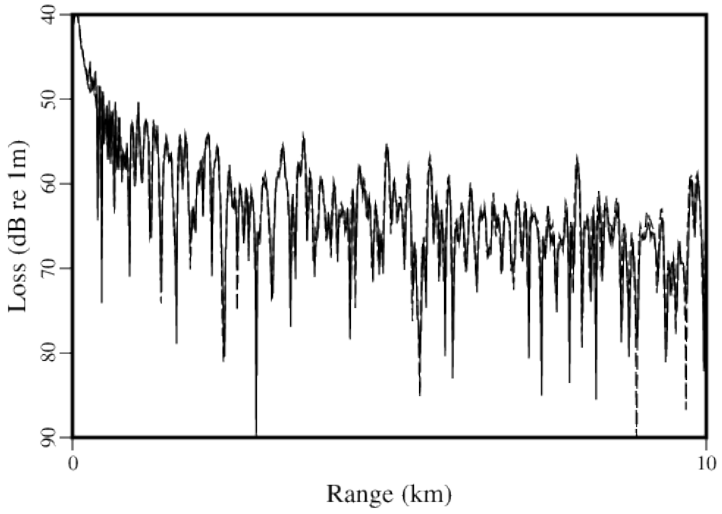

Figure 4.5: Transmission loss contours in RAM and RAMX with thick sediment for a frequency of 140 Hz. a) RAM, b)RAMX, c) comparison at receiver depth 250 meters: the dashed curve is RAMX.

frequencies: these results are representative. This environment has 400.5 meters of water overlying a 300.0 meter thick sediment layer which sits atop an elastic basement, all interfaces are horizontal and environmental parameters do not vary with range. The speed of sound in the water increases linearly with depth from 1475.0 m/s at the surface to 1525.0 m/s at 400.5 meters deep. The sediment has density 1.3 g/cm^3, sound speed that increases linearly with depth from 1700.0 m/s at the water-sediment interface to 1750.0 m/s at the sediment-basement interface, and has shear wave speed in RAMS that is varied in each plot. This sediment has properties similar to that of silty clays which have lower densities and sound speeds than most other sediment types [8]. The elastic basement has density 1.5 g/cm^3 and sound speed that increases with depth from 1800.0 m/s to 1850.0 m/s at 5000.0 meters deep. There is an attenuating layer beginning at 4000.0 meters deep. The source and receiver are at a depth of 100 meters.

As the shear speed in the sediment in RAMS is decreased, the RAMS and RAMX results become increasingly similar, with excellent agreement when the shear speed in the sediment is 200 m/s in RAMS as seen in 4.6(e), 4.8(e), and 4.10(e). RAMS loses accuracy at low shear speeds, and so the difference between RAMS and RAMX increases when the shear speed falls from 200 m/s to 50 m/s as seen in 4.6(f), 4.8(f), and 4.10(f). Plots showing a large part of the propagation environment for RAMX and RAMS with shear speed 200 m/s are seen in 4.7, 4.9, and 4.11.

4.4 A Third Sediment Treatment

RAM, RAMS, and RAMX are compared to the fluid-poro-elastic (FPE) solution developed by A. Metzler [9]. FPE allows for layered porous elastic sediments beneath a water layer and atop an elastic basement. We expect RAMS to compare reasonably well to FPE for low porosity sediment, as RAMS can account for the elasticity of the sediment layer. RAM and RAMX aren't expected to compare to FPE as well, both have fluid sediment layers that

do not account for the effects of elasticity. We expect RAMX to compare to FPE better than RAM as it can account for effects of elasticity in the underlying elastic solid layers.

We see the advantage RAMS has for high shear speed sediment layers in 4.12 and 4.14. In this environment there is 400.5 meters of water overlying a 300.0 meter thick sediment layer in 4.12 and 50.0 meter thick sediment layer in 4.14, atop a basement with higher sound speed, all interfaces are horizontal and environmental parameters do not vary with range. The speed of sound in the water increases linearly from 1475.0 m/s at the surface to 1525.0 m/s at the water-sediment interface. The sediment has density 1.7 g/cm^3 and sound speed 1700.0 m/s. The basement has sound speed 1800.0 m/s. In the RAMS results given in 4.12(b&e) and 4.14(b&e) the elastic basement has density 2.5 g/cm^3 and shear speed 800.0 m/s, the elastic sediment has shear speed 800.0 m/s. In the RAMX results given in 4.12(c&f) and 4.14(c&f) the elastic basement has density 2.5 g/cm^3 and shear speed 800.0 m/s. In the FPE results that RAM, RAMS, and RAMX are compared to in 4.12 and 4.14 the elastic basement has density 2.5 g/cm^3 and shear speed 800.0 m/s, and the porous elastic sediment is 10% porous. These sediment properties are similar to those of silty sand [8].The source is at a depth of 25.0 meters and the receiver is at a depth of 50.0 meters. The frequency varies between 4.12(a to c) and 4.12(d to f) at the same sediment thickness and again between 4.14(a to c) and 4.14(d to f).

As expected, RAMS matches best with FPE. Plots showing a large part of the propagation environment for RAMS are seen in 4.13 and 4.15. RAM and RAMX give very similar results, they are both out of pattern phase, especially with lower frequency sources. This displays the importance of sediment treatments: RAM and RAMX both treat the sediment as a fluid, failing to account for both the elasticity and porosity of the layer. There is no apparent improvement in the comparisons of RAM and RAMX to FPE as the environment and source frequency varies.

We expect RAMX to provide accurate acoustic predictions for sediments with low porosity and low shear speeds. Consider the same two environments, but with shear speed 200.0 m/s in the sediment in FPE. 4.16 shows comparisons between RAMX and FPE for a spectrum of porosity fractions (0.1, 0.2, 0.4, 0.6, 0.8, and 0.9) in the 50 meter thick sediment environment with source frequency 30 Hz. 4.17 shows comparisons between RAMX and FPE for a spectrum of porosity values in the 300 meter thick sediment environment with source frequency 50 Hz. As expected RAMX and FPE compare best when FPE has a low porosity sediment.

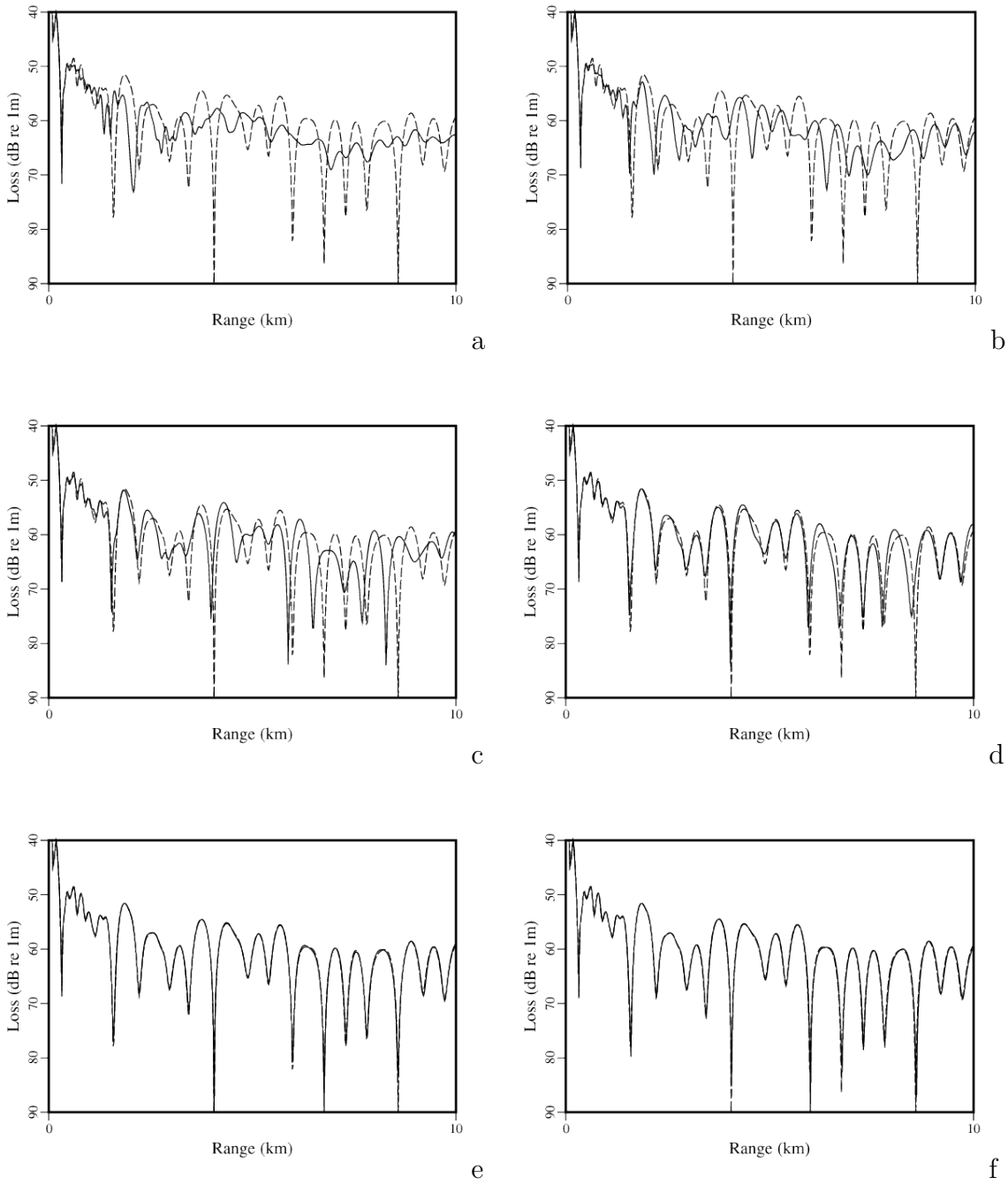

Figure 4.6: Transmission loss in RAMS and RAMX for a frequency of 25 Hz, RAMS has elastic sediment, RAMX has fluid sediment, the dashed curve is RAMX. The shear speed (in m/s) in the elastic sediment of RAMS is a)1000 b)800 c) 600 d)400 e)200 f)50

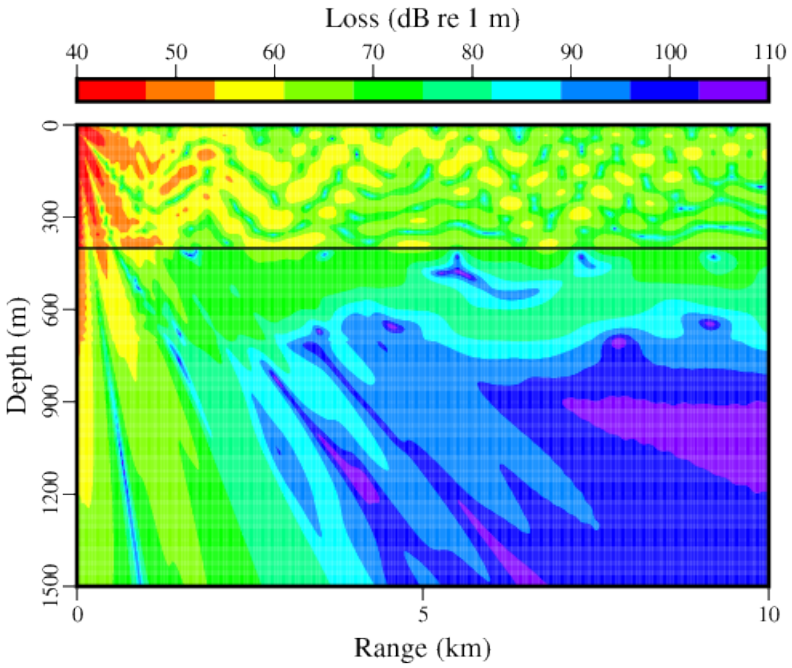

a

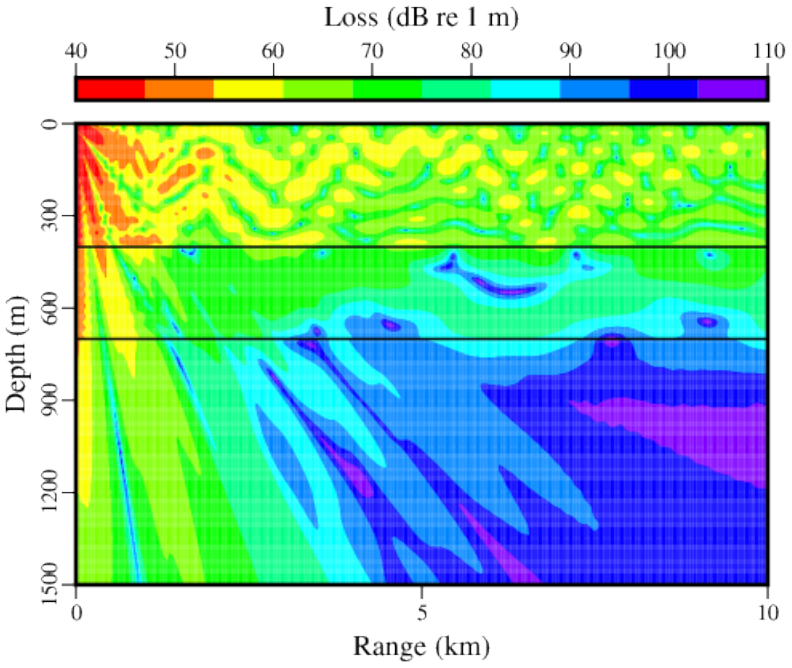

b

Figure 4.7: Transmission loss contours for a)RAMS and b)RAMX for a frequency of 25 Hz, RAMS has shear speed 200 m/s in the sediment layer

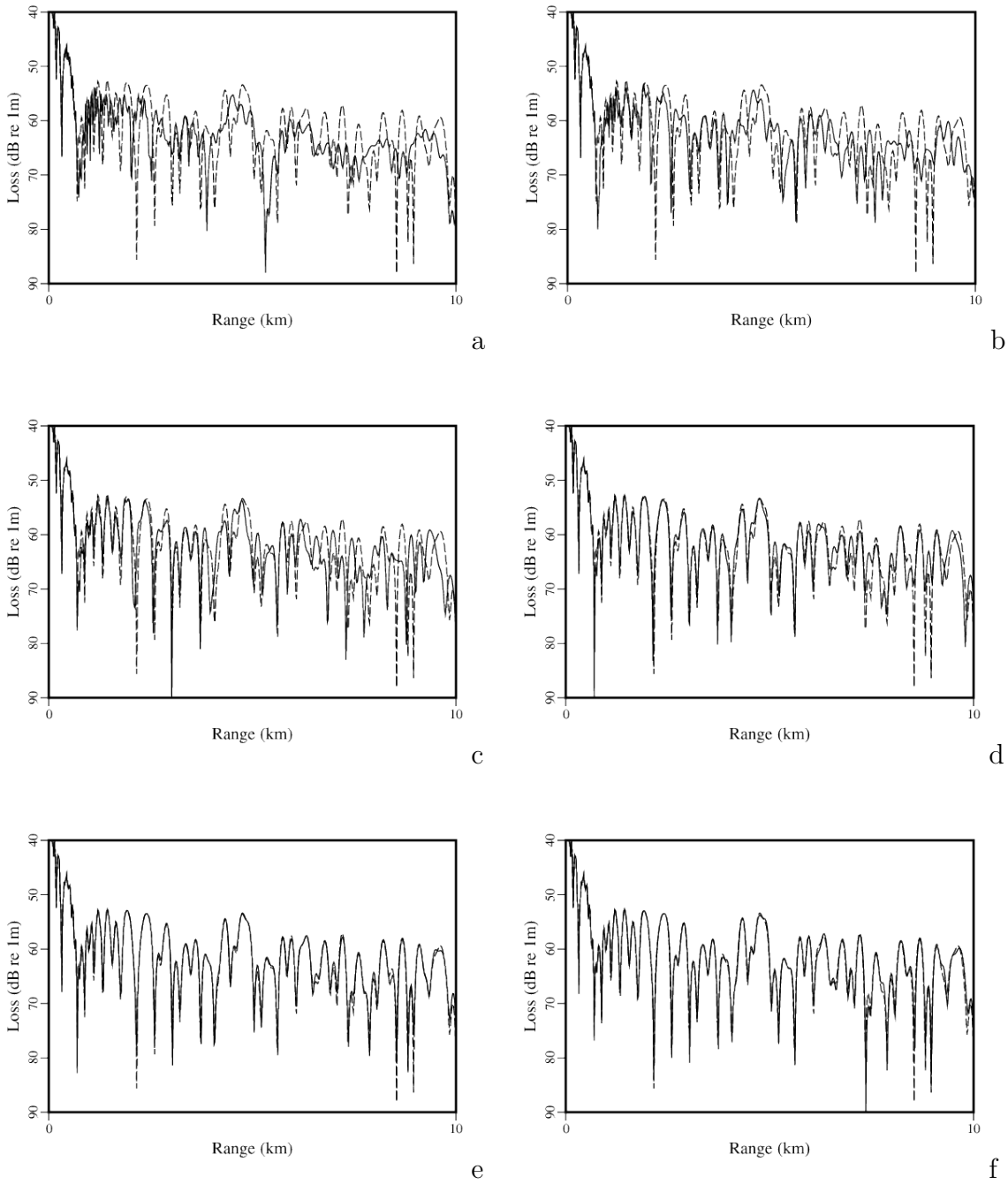

Figure 4.8: Transmission loss in RAMS and RAMX for a frequency of 50 Hz, RAMS has elastic sediment, RAMX has fluid sediment, the dashed curve is RAMX. The shear speed (in m/s) in the elastic sediment of RAMS is a)1000 b)800 c) 600 d)400 e)200 f)50

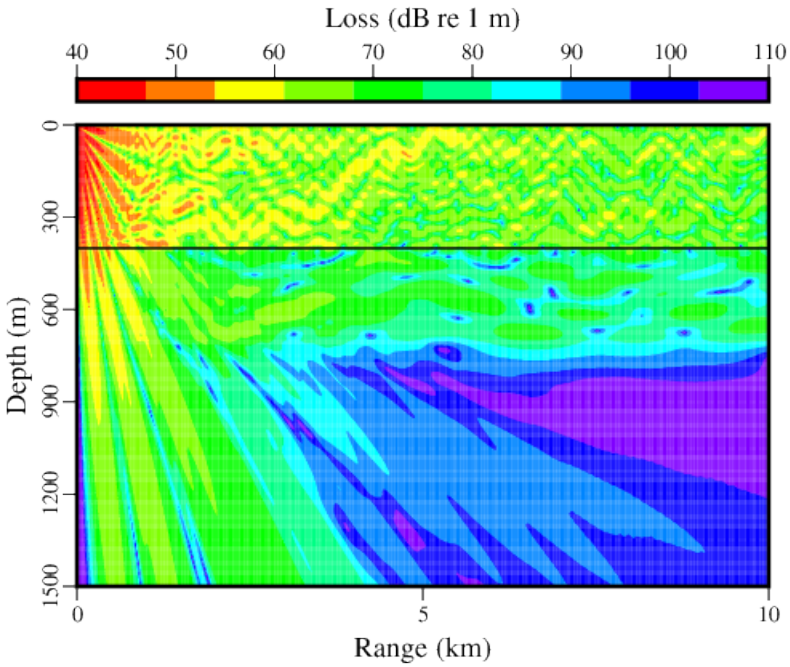

a

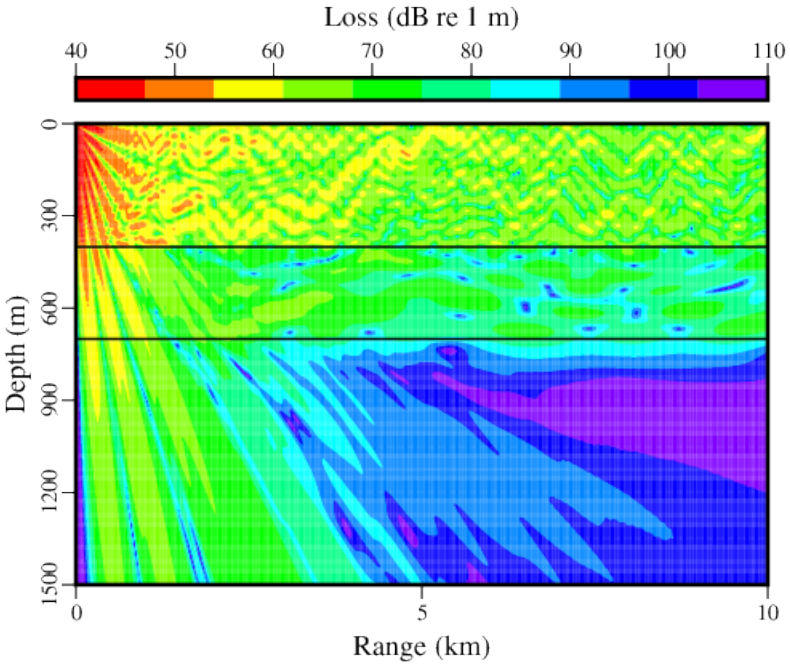

b

Figure 4.9: Transmission loss contours for a)RAMS and b)RAMX for a frequency of 50 Hz, RAMS has shear speed 200 m/s in the sediment layer

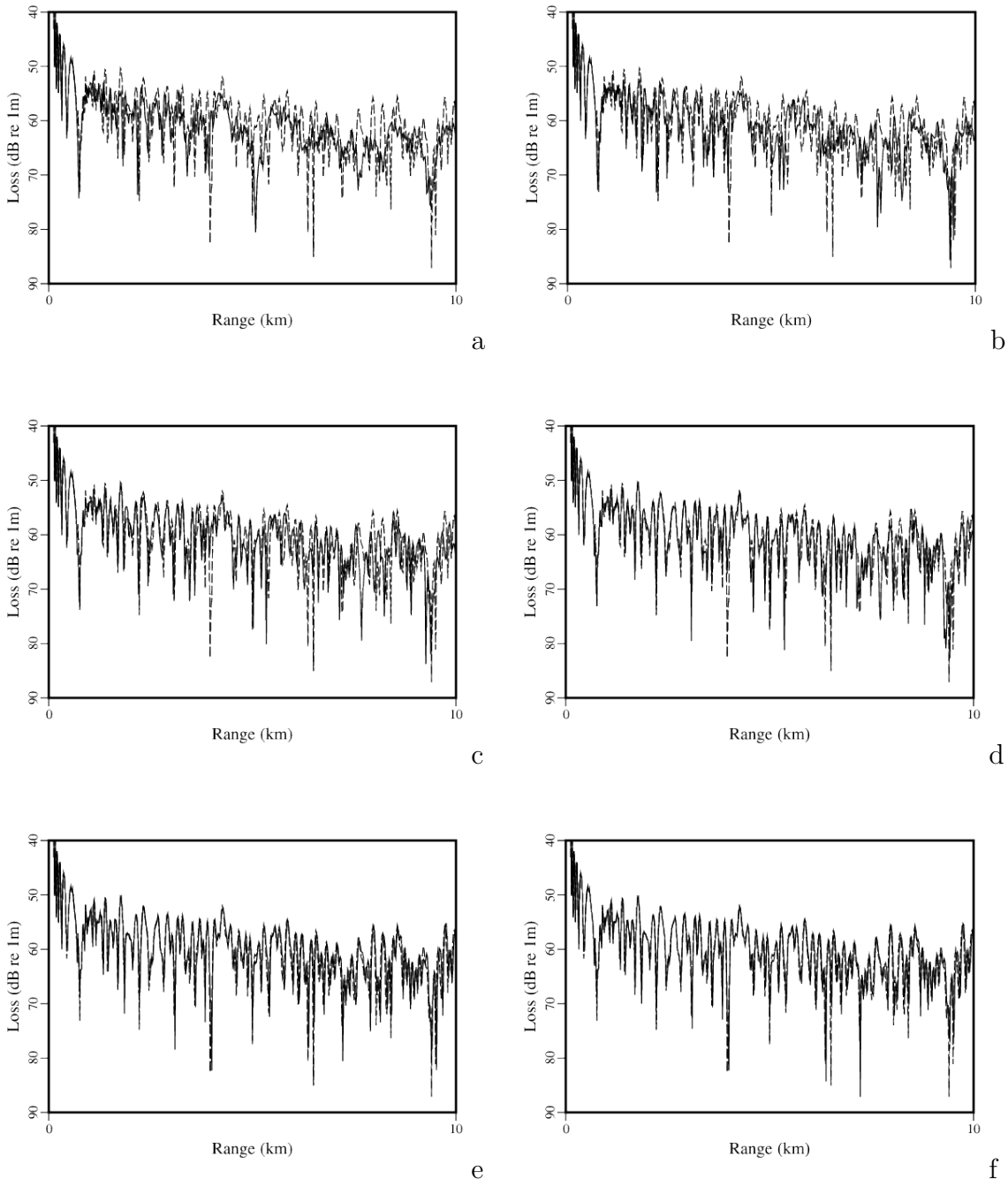

Figure 4.10: Transmission loss in RAMS and RAMX for a frequency of 100 Hz, RAMS has elastic sediment, RAMX has fluid sediment, the dashed curve is RAMX. The shear speed (in m/s) in the elastic sediment of RAMS is a)1000 b)800 c) 600 d)400 e)200 f)50

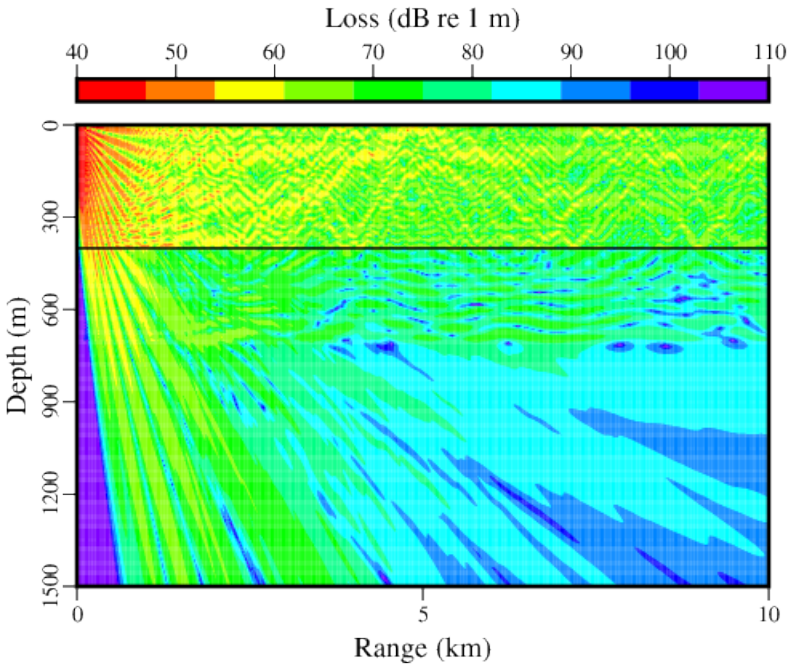

a

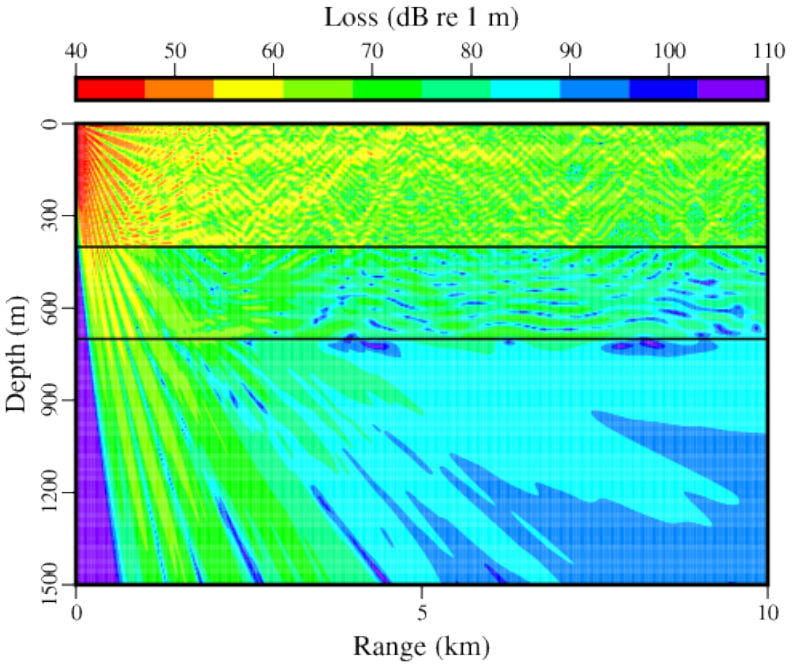

b

Figure 4.11: Transmission loss contours for a)RAMS and b)RAMX for a frequency of 100 Hz, RAMS has shear speed 200 m/s in the sediment layer

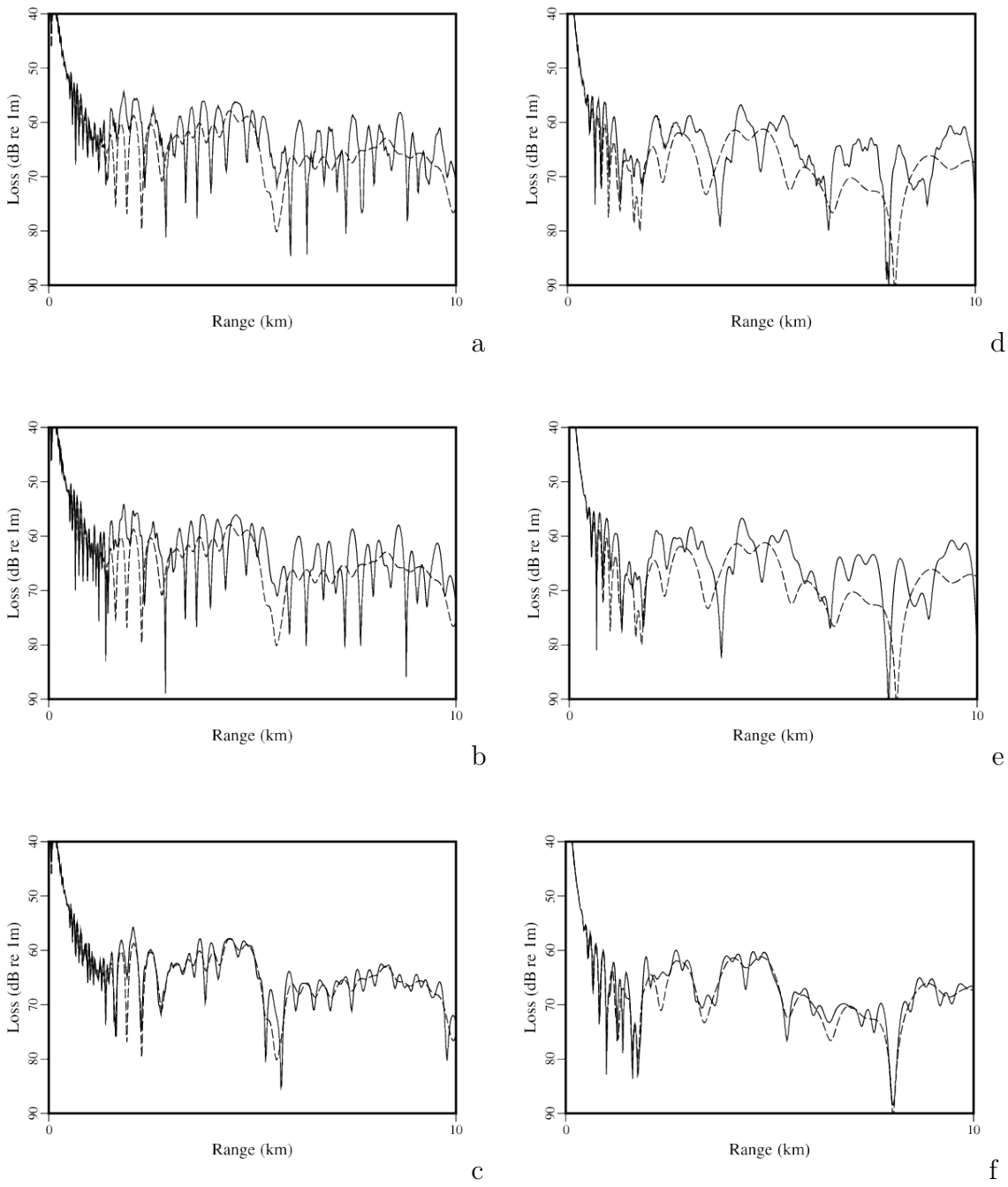

Figure 4.12: Transmission loss in RAM, RAMS, RAMX, and FPE with sediment thickness 300.0 meters and high shear speed in the sediments of RAMS and FPE. RAMS has elastic sediment, RAM and RAMX have fluid sediment, the dashed curve is FPE which has a porous elastic sediment. a&d)RAM b&e)RAMX c&f)RAMS. (a to c) have a frequency of 50 Hz and (d to f) have a frequency of 30 Hz.

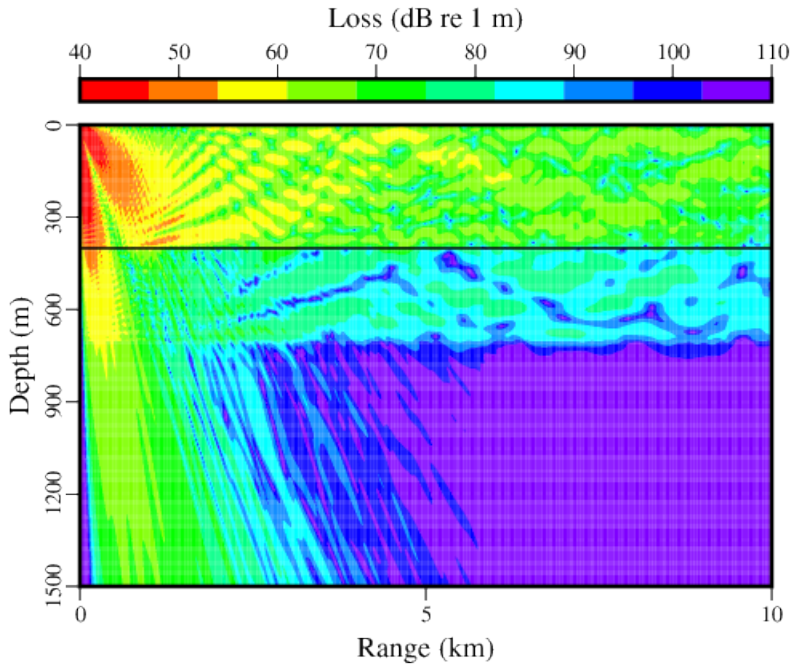

a

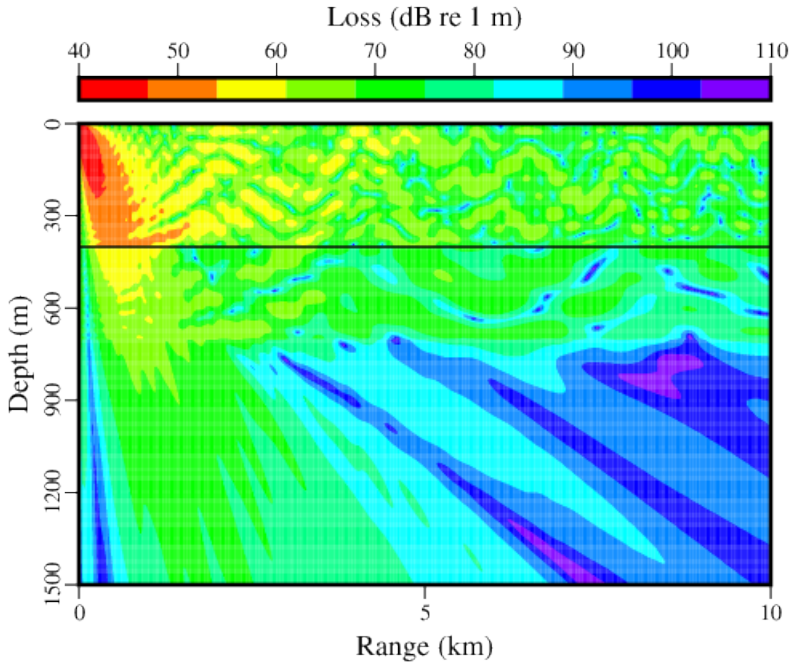

b

Figure 4.13: Transmission loss contours in RAMS with sediment thickness 300.0 meters, the source is at a depth of 25 meters. a)50 Hz b)30 Hz

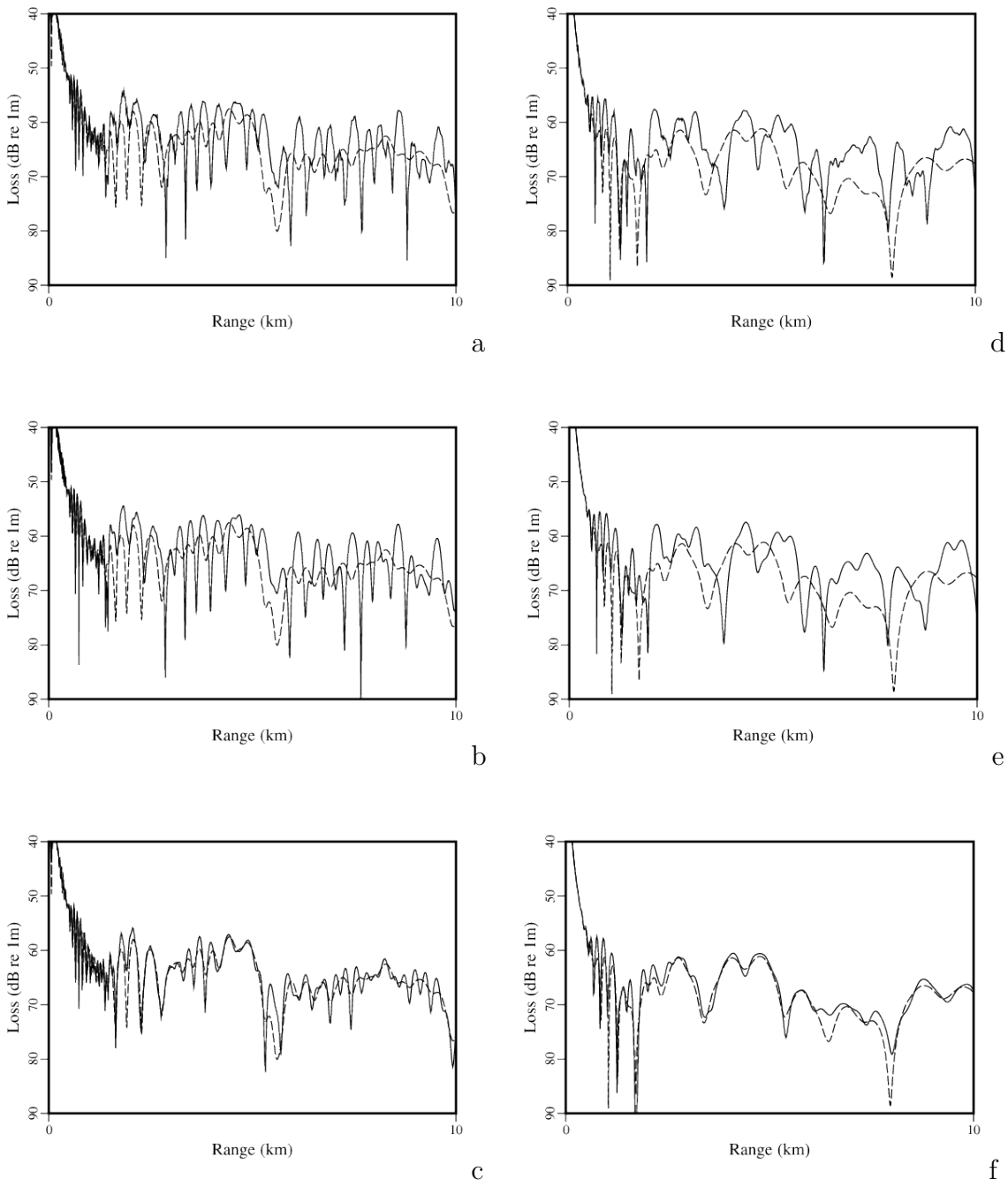

Figure 4.14: Transmission loss in RAM, RAMS, RAMX, and FPE with sediment thickness 50.0 meters and high shear speed in the sediments of RAMS and FPE. RAMS has elastic sediment, RAM and RAMX have fluid sediment, the dashed curve is FPE which has a porous elastic sediment. a&d)RAM b&e)RAMX c&f)RAMS. (a to c) have a frequency of 50 Hz and (d to f) have a frequency of 30 Hz.

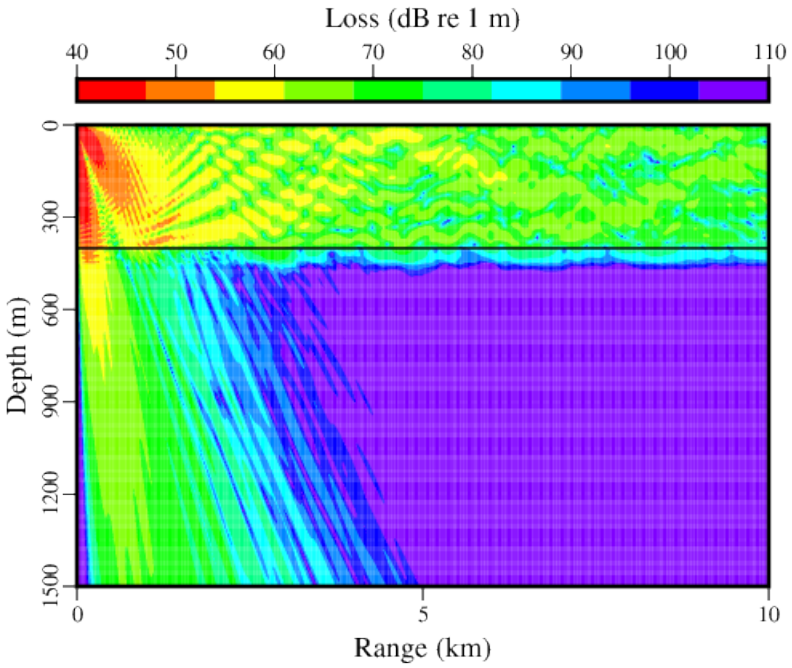

a

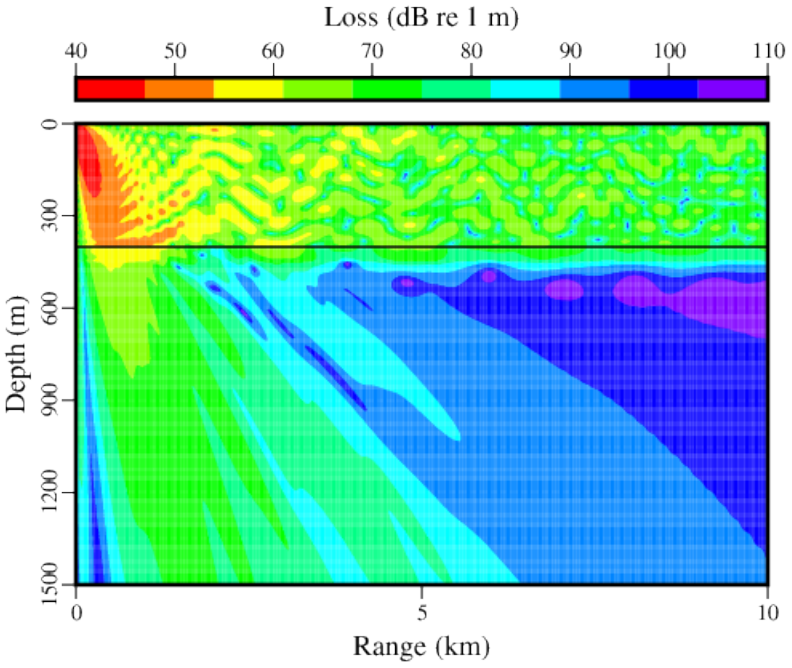

b

Figure 4.15: Transmission loss contours in RAMS with sediment thickness 50.0 meters, the source is at a depth of 25 meters. a)50 Hz b)30 Hz

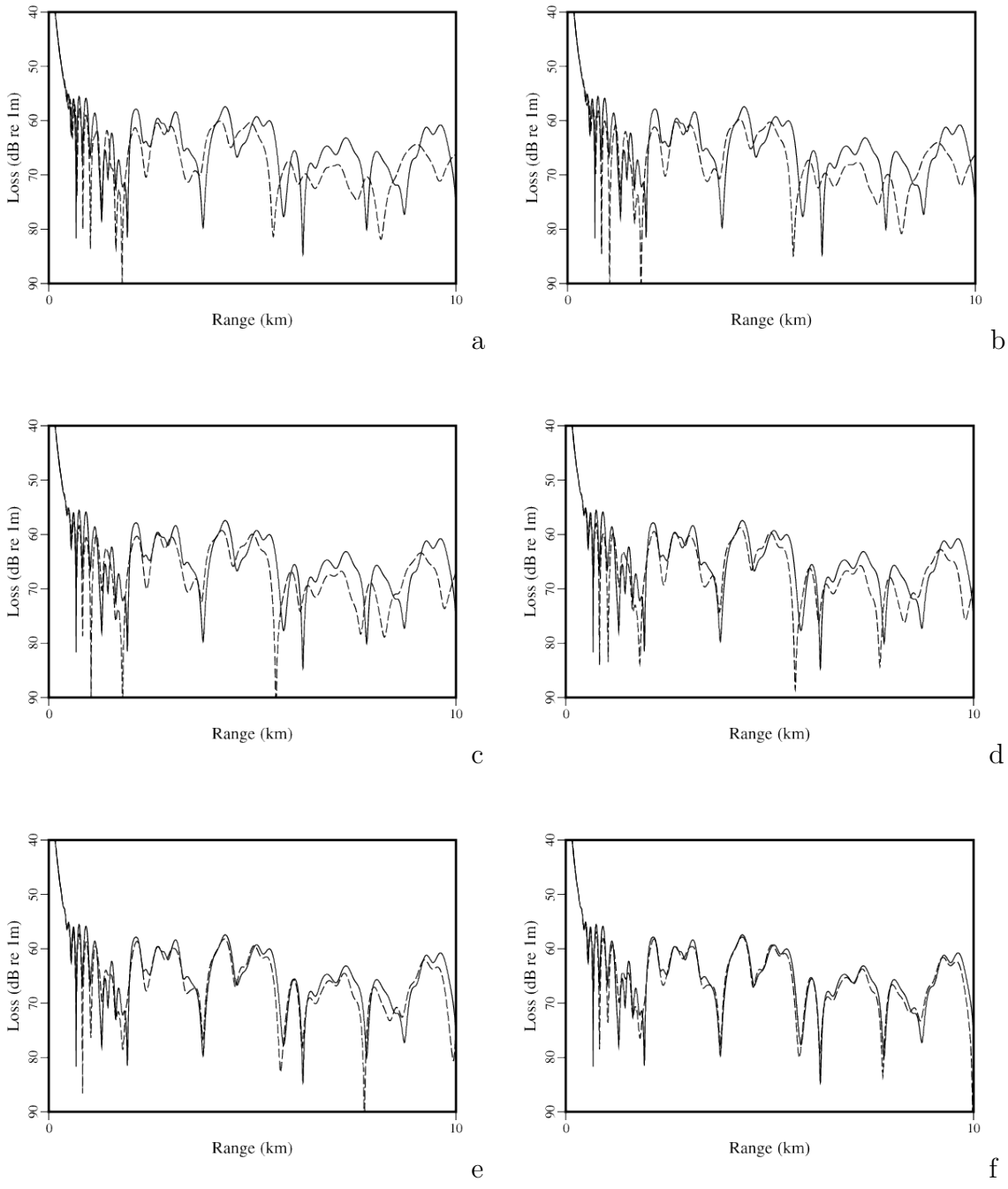

Figure 4.16: Transmission loss in RAMX and FPE with sediment thickness 50.0 meters and frequency 30 Hz, the dashed curve is FPE which has a porous elastic sediment with porosity fraction a)0.9 b)0.8 c)0.6 d)0.4 e)0.2 f)0.1

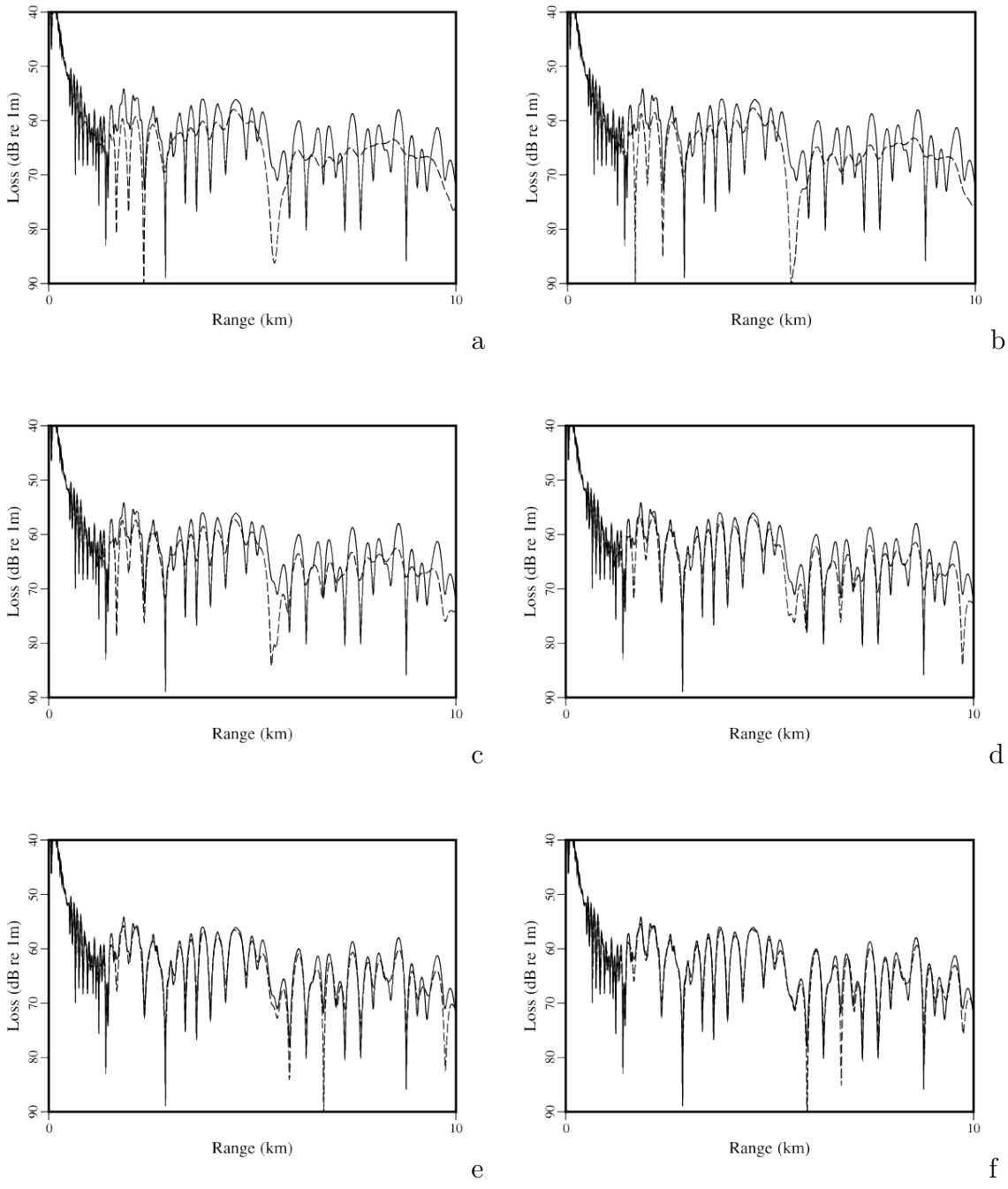

Figure 4.17: Transmission loss in RAMX and FPE with sediment thickness 300.0 meters and frequency 50 Hz, the dashed curve is FPE which has a porous elastic sediment with porosity fraction a)0.9 b)0.8 c)0.6 d)0.4 e)0.2 f)0.1

CHAPTER 5

CONCLUSION

We have successfully implemented the transitional solid sediment layer in a parabolic equation solution. RAMX compares well with its predecessors RAM and RAMS in limiting cases, indicating that the new fluid-fluid interface has been accurately accounted for. RAMX compares well to two alternate sediment treatments, elastic and poro-elastic when the elasticity or poro-elasticity are low. The comparisons improve as the shear speed in RAMS decreases and as the porosity fraction in FPE decreases for fixed low sediment shear speed. These comparisons show that RAMX is a valid, functional solution. RAMX is expected to give accurate predictions of acoustic interactions with sediments whose properties approach that of a fluid, transitional solids. Transitional solid sediment layers - such as sands, silts, clays and muds, are common - as are other sediment types that should be treated differently in mathematical models. The implementation of variable density in the upper propagation environment allows for sound propagation prediction in environments without any water or water with non-unity density, a feature not available in RAM or RAMS. RAMX retains the ability to model elastic sediment and basement layers from RAMS with the added functionality of an additional fluid sediment layer. Additional fluid layers could be added following the same approach. Accurately modeling the sediment layer in a geoacoustic model is of great importance, the work presented here is a step toward accurately treating all sediment types and layerings. Models for other sediment treatments, such as poro-acoustic, exist and provide accurate predictions for sound interaction in sediments with appropriate properties.

Errors in the new implementation arise from the assumption made in enforcing interface conditions that the interface lies at the midpoint of two grid points, which not generally true. The results suggest that these errors are small.

5.1 Future Work

Some single error measure across models would be useful for comparing models and convergence testing in a particular model. RAMX combines the features of RAM and RAMS, adding the option of porosity to RAMX would make for a more physically accurate model. Similar changes should be made to a $\langle u_x, w \rangle$ formulation of the parabolic equation solution, these formulations have been shown to be more accurate than the $\langle \Delta, w \rangle$ formulation presented here [10]. The ability to account for multiple fluid sediment layers and sediment layers that are not parallel would allow for more accurate modeling of sound propagation in the ocean.

REFERENCES CITED

[1] F. Jensen W. Kuperman M. Porter H. Schmidt. *Computational Ocean Acoustics*. Springer, La Spezia, Italy, 2005.

[2] J. Becker and D. Sandwell. Global estimates of seafloor slope from single-beam ship soundings. *Journal of Geophysical Research*, 113:C05028, 2008.

[3] W. Jerzak. *Parabolic Equations for Layered Elastic Media*. PhD thesis, Rensselaer Polytechnic Institute, August 2001.

[4] M. Collins. User's guide for ram versions 1.0 and 1.0p. `ftp://ftp.apl.washington.edu/archive/whales/Haro_Strait/rrsfc/ram.pdf`. Accessed: April 2013.

[5] R.A. Zingarelli and D.B. King. Ram to navy standard parabolic equation: Transition from research to fleet acoustic model. `http://www.nrl.navy.mil/research/nrl-review/2003/simulation-computing-modeling/zingarelli/`. Accessed: April 2013.

[6] M. Collins. A higher-order parabolic equation for wave propagation in an ocean overlying an elastic bottom. *J. Acoust. Soc. Am.*, 86:1459–1464, 1989.

[7] S. Frank, R. Odom, and J. Collis. Elastic parabolic equation solutions for underwater acoustic problems using seismic sources. *J. Acoust. Soc. Am.*, 133:1358–1367, 2013.

[8] E. Hamilton. Geoacoustic modeling of the sea floor. *J. Acoust. Soc. Am.*, 68:1313–1340, 1980.

[9] A. Metzler, W. Siegmann, M. Collins, and J. Collis. Two parabolic equations for propagation in layered poro-elastic media. *J. Acoust. Soc. Am.*, (Prepublication), 2013.

[10] D. Outing. *Parabolic Equation Methods for Range Dependent Layered Elastic Media*. PhD thesis, Rensselaer Polytechnic Institute, April 2004.

[11] S. McDaniel. Application of the parabolic approximation to predict acoustical propagation in the ocean. *American Journal of Physics*, 47:64–68, 1979.

APPENDIX A - FORMAL SOLUTION

Consider the partial differential equation (PDE)

$$\frac{\partial}{\partial r} f(r,z) = Z f(r,z)$$

where Z is a differential operator in z only. Differentiating with respect to r and substituting in the original PDE to the right hand side yields

$$\frac{\partial^2 f}{\partial r^2} = Z^2 f$$

where the exponent on Z indicates a repeated operation. Differentiate and substitute repeatedly to obtain

$$\frac{\partial^n f}{\partial r^n} = Z^n f.$$

Now consider the Taylor series

$$f(r+\Delta r, z) = \sum_{n=0}^{\infty} \frac{(\Delta r)^n}{n!} \frac{\partial^n f(r,z)}{\partial r^n} = \sum_{n=0}^{\infty} \frac{(\Delta r)^n}{n!} Z^n f(r,z) = \left(\sum_{n=0}^{\infty} \frac{(\Delta r Z)^n}{n!} \right) f(r,z).$$

Recognizing the Taylor series for $e^{\Delta r Z}$ yields the formal solution

$$f(r+\Delta r, z) = e^{\Delta r Z} f(r,z).$$

This solution is useful for a variety of problems, especially in developing numerical solution schemes as it allows f to be calculated at any range given f at some 'earlier' range[11].

APPENDIX B - ALTERNATE METHOD FOR SATISFYING INTERFACE CONDITIONS WHEN THE INTERFACE LIES ON A GRID POINT

Consider the same problem laid out in 3.1 with the interface lying on $x_m = s$. The first interface condition gives $u_m^{(a)} = u_m^{(b)}$. A single nonphysical-value will appear in the discretization of the second derivative when $j = m$, it will be $u_{m-1}^{(b)}$ if the discretization is centered in $[s, 2]$. Discretely approximate the interface conditions as:

$$\frac{u_{m+1}^{(a)} + u_{m-1}^{(a)}}{2} = \frac{u_{m+1}^{(b)} + u_{m-1}^{(b)}}{2}$$

and

$$\alpha \frac{u_{m+1}^{(a)} - u_{m-1}^{(a)}}{2\Delta x} = \beta \frac{u_{m+1}^{(b)} - u_{m-1}^{(b)}}{2\Delta x}.$$

These approximations are centered around the interface. Solving for the two unknown, nonphysical-values gives

$$u_{m+1}^{(a)} = \frac{2\beta}{\alpha + \beta} u_{m+1}^{(b)} + \frac{\alpha - \beta}{\alpha + \beta} u_{m-1}^{(a)} \tag{B.1}$$

and

$$u_{m-1}^{(b)} = \frac{\beta - \alpha}{\alpha + \beta} u_{m+1}^{(b)} + \frac{2\alpha}{\alpha + \beta} u_{m-1}^{(a)}. \tag{B.2}$$

Inserting (B.2) into the discretization

$$\frac{u_{m-1}^{(b)} - 2u_m^{(b)} + u_{m+1}^{(b)}}{\Delta x^2} \approx f_m$$

yields

$$\frac{2\alpha}{\alpha + \beta} u_{m-1}^{(a)} + u_m + \frac{2\beta}{\alpha + \beta} u_{m+1}^{(b)} \approx \Delta x^2 f_m.$$

Two entries in the matrix will need to be updated to reflect this change.

A result with this alternate approach is shown in B.1 with absolute error shown in B.2. This example has $\alpha = 1$, $\beta = 2$, and $s = 1$ as in Section 3.1.

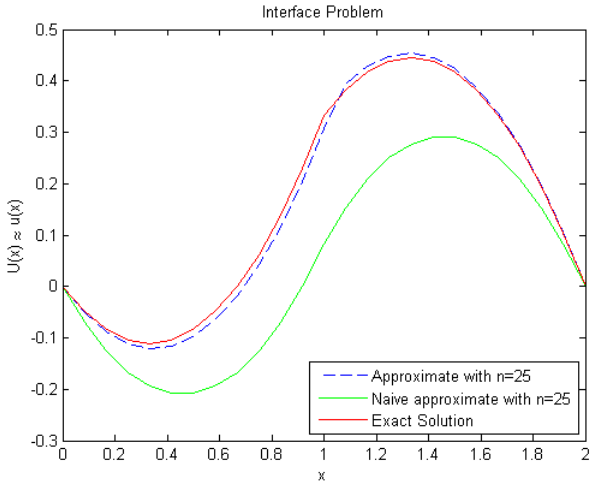

Figure B.1: Numerical approximations with the interface on a grid point

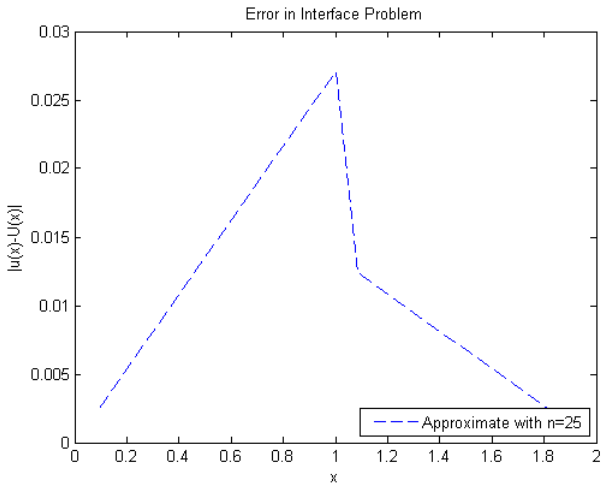

Figure B.2: Error in numerical approximation with the interface on a grid point